Counterflow-induced clustering: Exact results

Amit Kumar Chatterjee [1,*] and Hisao Hayakawa [1,2,†]

[1] *Yukawa Institute for Theoretical Physics, Kyoto University, Kitashirakawa Oiwakecho, Sakyo-ku, Kyoto 606-8502, Japan*

[2] *Center for Gravitational Physics and Quantum Information, Yukawa Institute for Theoretical Physics, Kyoto University, Kitashirakawa Oiwakecho, Sakyo-ku, Kyoto 606-8502, Japan*

(Received 7 August 2022; accepted 27 April 2023; published 22 May 2023)

We analyze the cluster formation in a nonergodic stochastic system as a result of counterflow, with the aid of an exactly solvable model. To illustrate the clustering, a two species asymmetric simple exclusion process with impurities on a periodic lattice is considered, where the impurity can activate flips between the two nonconserved species. Exact analytical results, supported by Monte Carlo simulations, show two distinct phases, *free-flowing phase* and *clustering phase*. The clustering phase is characterized by constant density and vanishing current of the nonconserved species, whereas the free-flowing phase is identified with nonmonotonic density and nonmonotonic finite current of the same. The n-point spatial correlation between n consecutive vacancies grows with increasing n in the clustering phase, indicating the formation of two macroscopic clusters in this phase, one of the vacancies and the other consisting of all the particles. We define a *rearrangement parameter* that permutes the ordering of particles in the initial configuration, keeping all the input parameters fixed. This rearrangement parameter reveals the significant effect of nonergodicity on the onset of clustering. For a special choice of the microscopic dynamics, we connect the present model to a system of run-and-tumble particles used to model active matter, where the two species having opposite net bias manifest the two possible run directions of the run-and-tumble particles, and the impurities act as tumbling reagents that enable the tumbling process.

DOI: 10.1103/PhysRevE.107.054905

I. INTRODUCTION

Clustering of nonattractive elements is an intriguing phenomenon occurring in diverse areas of science and society. It appears in various fields such as granular materials [1–3], vehicular and pedestrian traffic flows [4–7], active matter [8,9], biology [10,11], etc. At the heart of the clustering phenomena lies a transition between free-flowing phase and jammed phase where motion becomes highly restrictive, as some suitable system parameter is tuned. The tuning parameter for granular material is packing fraction, it is car or pedestrian density for traffic flow and self-propulsion force in case of dense active matter. In fact, a jamming phase diagram has been proposed keeping in mind the generality of such transitions [1] and there are experiments conducted on colloidal particles supporting the concept of this generic phase diagram such as Ref. [12]. The control of clustering is important in daily life. Indeed, understanding the formation of jamming and finding ways to transit to unjammed state, has immense importance in traffic science. The other applications include occurrence of cellular jamming transitions in cancer [10,11]. Analysis of clustering, as a phase transition in interacting many body systems, constitutes an interesting topic from the physics point of view. Thus, it seems natural to investigate the clustering phenomena through the lens of statistical mechanics.

One possible mechanism of clustering is the presence of counterflow in a system. Counterflows arise naturally in real life situations, e.g., pedestrian traffic flow [7] in narrow lanes, busy pedestrian zones, crossings between two footpaths, etc. In these situations, we often observe pedestrians moving in opposite directions, automatically create counterflow situations. Counterflows in pedestrian dynamics can result in interesting phenomena like traffic jam at high densities [13,14], self-organized lane formations [15,16], oscillatory changes in the dominant direction of motion at bottlenecks [17]; as well as unexpected events like panic and crowd disasters [18]. Interesting experimental results regarding counterflows have revealed that the total flow in a counterflow situation can be greater than the sum of the two comparable unidirectional flows [16,19]. Numerical studies show that the existence of counterflowing agents ignoring traffic rules can surprisingly lower the possibility of traffic jam [20]. Apart from the pedestrian dynamics, counterflow occurs in nature and has been incorporated in industries. In fact, countercurrent exchange of heat or chemicals between two oppositely flowing fluids (i.e., counterflow situation), has been proved to be much more efficient than cocurrent exchange of the same between two parallel flowing fluids. Such principles are often used to devise heat exchangers [21] used in industries and are found in nature, e.g., salt glands in sea and desert birds [22,23], mammalian kidneys [24], etc.

In the context of cluster formation resulting from counterflow, spontaneous symmetry breaking in a model with two oppositely moving particles with exchange interaction, has been discussed with periodic boundaries [25,26] and open

*ak.chatterjee@yukawa.kyoto-u.ac.jp
†hisao@yukawa.kyoto-u.ac.jp

boundaries [27]. Notably, later it has been proved that the spatial condensation of particles under periodic boundary condition [26] is not associated with a phase transition in the grand canonical ensemble [28,29]. There exist several models in nonequilibrium statistical mechanics that exhibit phase transitions in one dimension [30–41]. However, considerably few one-dimensional nonequilibrium models with simplified local dynamics, are amenable to exact analytical calculations which provide much insights to the microscopic origins of the phase transitions [36,40–43]. In context of cluster formations in exactly solvable disordered systems, Bose-Einstein condensates have been studied in multispecies asymmetric simple exclusion processes [44,45], utilizing matrix product ansatz [46] and zero range process [47,48]. Traffic jam in more realistic traffic models, like bus route models, has been considered [49,50], and its connection to Nagel-Schreckenberg model of traffic flow has been explored in details [51]. There are various other interesting studies of one-dimensional traffic flows under periodic boundary conditions [4–7,52–55]. Notably, once a formed cluster is stable and moves in one direction, it is similar to the time crystal [56–60]. To avoid such clustering, model with bypassing defects through long-range hopping, has been analyzed [61]. Notably, exact analytical results showing clustering phenomenon has been considerably few.

Recently, clustering of self-propelled objects like bacteria have gained much attention [62,63]. Such active matter can exhibit motility-induced phase separation by accumulating in regions with slow movement [64–66], or they can aggregate near chemical nutrients [63]. The motion of self-propelled objects including bacteria, is often described by run-and-tumble particles (RTPs) [67–74]. Analytical solutions of run-and-tumble models are few, including exact solution for one and two RTPs [69–73], mean-field analysis of many interacting RTPs [75] and approximate solution for restricted RTPs [73]. The tumbling dynamics corresponds to occasional change in direction of motion, which specifically in one dimension would correspond to *flip* between right and left moving objects. Thus, it would be interesting to ask how to accommodate such flip dynamics of RTPs in simple lattice models that are exactly solvable, contain many interacting RTPs and exhibit clustering.

In this work, we provide exact results showing cluster formation on a one-dimensional periodic lattice, when counterflow and flip dynamics are present in the system. As a model, we consider the two species asymmetric simple exclusion process with impurity activated flips (2-ASEP-IAF) [76]. We show the existence of two different phases, namely, the *free-flowing phase* and the *clustering phase*, and characterize them using observables like average density, drift current and spatial correlations, obtained analytically and supported by Monte Carlo simulations. Interestingly, in the counterflow situation, with a special choice of the microscopic hop rates, the 2-ASEP-IAF can be interpreted as a system of many RTPs in presence of tumbling reagents. Since the RTPs have been extremely useful to model active matter on lattices, we would discuss separately the clustering in this special case in some details. Also, the 2-ASEP-IAF has plausible mappings to two-lane ASEP with bridges [76] and enzymatic chemical reactions [76], explained briefly in the next section.

In Sec. II we define the model and briefly describe its connection to the two-lane model, enzymatic chemical reactions and RTPs. Section III describes the steps to obtain the exact matrix product steady state of the model with infinite-dimensional matrices. The model being nonergodic, we state the choice of initial configuration considered here in Sec. IV and calculate the partition function showcasing the important steps. In Sec. V we discuss in details the analytical results for density, current and spatial correlations which establish the existence of two different phases. The role of initial configurations on the onset of the clustering, is investigated in Sec. VI. The special constraint on the microscopic rates, for which the 2-ASEP-IAF can be mapped to a model of run-and-tumble particles, is analyzed in detail in Sec. VII. We summarize our main results and future directions in Sec. VIII. Appendix A provides expressions and brief derivations of some observables. The explicit form of the density-fugacity relation and a special case that leads to a closed form solution of the fugacity, are presented in Appendix B. In Appendix C we clarify on the variations of the initial configuration considered in the main text, that can give rise to similar clustering. We show the convergence of our results with system size in Appendix D. The comparison of our model to the Arndt-Heinzel-Rittenberg model of counterflow, is briefly discussed in Appendix E.

II. MODEL

We consider two different species (1 and 2) along with impurities (+) and vacancies (0) on a one-dimensional periodic lattice with L sites, $i = 1, 2, \ldots, L$. Species 1 and species 2 can hop to right with rates p_1 and p_2, respectively, or to left with rates q_1 and q_2, respectively, if the target site is vacant. The motion of the impurity is restricted only toward right, with rate ϵ. The unidirectional motion of the impurity is a characteristic that differentiates it from the two species. Further, this assumption turns out to be crucial to obtain the exact steady-state probability distribution. Alongside the hopping dynamics, species 1 and 2 can transform into each other with rates w_{12} and w_{21}, such flipping being activated only in presence of impurity. Following the nomenclature of Ref. [76], we refer this model as 2-ASEP-IAF, where ASEP represents asymmetric simple exclusion process and IAF stands for impurity activated flips. The microscopic dynamics of 2-ASEP-IAF is represented as

$$10 \underset{q_1}{\overset{p_1}{\rightleftharpoons}} 01, \quad 20 \underset{q_2}{\overset{p_2}{\rightleftharpoons}} 02,$$
$$+0 \xrightarrow{\epsilon} 0+, \quad 1+ \underset{w_{21}}{\overset{w_{12}}{\rightleftharpoons}} 2+. \tag{1}$$

The 2-ASEP-IAF can be restated as a four-state model where each lattice site can be in either of the four possible states 1 or 2 or + or 0. The input parameter space for the model contains several parameters, more precisely given by $(p_1, p_2, q_1, q_2, \epsilon, w_{12}, w_{21}, \rho_0, \rho_+)$. The parameters $\rho_0 = N_0/L$ and $\rho_+ = N_+/L$ are the conserved densities of the vacancies and the impurities, respectively, with N_0 and N_+ being the number of vacancies and impurities in the system. In this paper, we aim to investigate the effect of counterflow

on the system, and to do so, we pick out q_1 to be the tuning parameter, keeping all other rates fixed. We fix $p_2 > q_2$ (apart from the discussion in Sec. VII) and $\epsilon > 0$. Subsequently, if $q_1 < p_1$, all particles have net bias along the same direction, keeping the system in *natural flow* situation. However, when $q_1 > p_1$, species 1 has net bias in the direction opposite to the net bias of species 2 and impurities, thereby species 1 opposes the motion of other components and creates a *counterflow* situation. Since the tuning parameter q_1 can control the flow situation in the system, we denote it as the *counterflow parameter*.

We mention three interesting plausible mappings of the present model [Eq. (1)] to other systems of interest. These three systems, as briefly explained below, are (i) run-and-tumble particles, (ii) enzymatic chemical reaction, and (iii) two-lane ASEP.

(i) To study active matter on lattices, run-and-tumble particles (RTPs) constitute useful models [68], notably with considerably few analytical results [69–74]. The RTPs keep moving along a particular direction until they tumble, i.e., change the direction of motion. The two different species having net bias toward opposite directions in 2-ASEP-IAF, can be considered as two possible orientations of the RTP, only if the counterflow situation is considered. Basically the RTP is a two-state particle where its two possible states or run directions are imitated by species 1 and 2 of the 2-ASEP-IAF. A particularly relevant case is when $p_2 - q_2 = q_1 - p_1$, i.e., the RTP moves with same speed in both directions with intermediate tumbling, in accordance with the recently proposed restricted tumbling model [73] and the continuum active random walk model [74]. Notably, in our mapping, the impurities act as the mediators for the tumbling process. This special case which maps the 2-ASEP-IAF to RTPs, would be discussed in more details in Sec. VII.

(ii) The 2-ASEP-IAF can be connected to an enzymatic chemical reaction in a narrow channel of diffusing chemical reagents. In this case, the impurity represent the enzymes which initiate the reaction between substrate and products, that amounts to the flip dynamics in the present model [76].

(iii) The 2-ASEP-IAF can be mapped to a two-lane ASEP, a simple model for two-lane traffic flow, where the species 1 and 2 play the roles of particles hopping with different rates in the two different lanes and the impurities in 2-ASEP-IAF mimic the bridges connecting the two lanes in the two-lane ASEP [76]. Thus the flip dynamics between two species activated by impurities represent the lane change dynamics of the particles in the two-lane ASEP model.

Due to such connections of the 2-ASEP-IAF to several other important models, we study analytically the possibility of cluster formation in the model in presence of counterflow, which can possibly provide information about clustering in the connected models.

III. STEADY STATE

The probability $P(\{s_i\})$ of any configuration $\{s_i\}$ ($s_i = 1$ or 2 or 0 or $+$, denoting the constituent at site i), in the nonequilibrium steady state corresponding to the microscopic dynamics Eq. (1), is obtained in the following matrix product form:

$$P(\{s_i\}) \propto \mathrm{Tr}\left[\prod_{i=1}^{L} X_i\right],$$
$$\text{where} \quad X_i = D_1\delta_{s_i,1} + D_2\delta_{s_i,2} + A\delta_{s_i,+} + E\delta_{s_i,0}. \quad (2)$$

In Eq. (2), the matrix X_i represents the component s_i at site i and $\delta_{(..)}$ is Kronecker δ symbol. Specifically, the matrices D_1, D_2, E, A correspond to species 1, species 2, vacancy, and impurity, respectively. The configurations of the system evolve according to the master equation

$$\frac{d|P(t)\rangle}{dt} = M|P(t)\rangle, \quad (3)$$

where the matrix M is the rate matrix containing transition rates between configurations and $|P(t)\rangle$ is the column vector whose elements are time dependent probabilities $P(\{s_i\}, t)$ for all possible configurations $\{s_i\}$. In the steady state, the probabilities $P(\{s_i\}, t)$ converge to the time independent values $P(\{s_i\})$ mentioned in Eq. (2). For 2-ASEP-IAF with two-site local dynamics [Eq. (1)], the rate matrix can be decomposed as

$$M = \sum_{i=1}^{L} (I \otimes \ldots I \otimes \mathcal{M}_{i,i+1} \otimes I \cdots \otimes I), \quad (4)$$

where $\mathcal{M}_{i,i+1}$ is a 16×16 matrix acting on the pair of sites $(i, i+1)$ and I is 4×4 identity matrix placed at every site except the pair $(i, i+1)$. In steady state $M|P\rangle = 0$. The steady state can be achieved using the following two-site flux-cancellation condition

$$\mathcal{M}_{i,i+1}\mathbf{X}_i \otimes \mathbf{X}_{i+1} = \tilde{\mathbf{X}}_i \otimes \mathbf{X}_{i+1} - \mathbf{X}_i \otimes \tilde{\mathbf{X}}_{i+1}, \quad (5)$$

where

$$\mathbf{X} = (E, A, D_1, D_2)^T,$$
$$\tilde{\mathbf{X}} = (\tilde{E}, \tilde{A}, \tilde{D}_1, \tilde{D}_2)^T, \quad (6)$$

where $(.)^T$ denotes the transpose of the row vector (.) and $\tilde{E}, \tilde{A}, \tilde{D}_1.\tilde{D}_2$ are auxiliary matrices that are introduced to satisfy the steady-state equation and these have to be found out consistently along with the matrix representations for E, A, D_1, D_2. We find that suitable choices for the auxiliary matrices in this case are

$$\tilde{E} = 1, \ \tilde{A} = 0, \ \tilde{D}_1 = 0, \ \tilde{D}_2 = 0. \quad (7)$$

Using the above choices of the auxiliary matrices in Eq. (5), we arrive at the following matrix algebra:

$$p_1 D_1 E - q_1 E D_1 = D_1,$$
$$p_2 D_2 E - q_2 E D_2 = D_2,$$
$$\epsilon A E = A,$$
$$w_{12} D_1 A = w_{21} D_2 A. \quad (8)$$

We find that Eq. (8) is satisfied by the infinite-dimensional matrix representations given below:

$$E = \begin{pmatrix} 0 & 0 & 0 & 0 & . & . \\ 1 & 0 & 0 & 0 & . & . \\ 0 & 1 & 0 & 0 & . & . \\ 0 & 0 & 1 & 0 & . & . \\ 0 & 0 & 0 & 1 & & \\ . & . & & & . & \\ . & . & & & & . \end{pmatrix},$$

$$A = \begin{pmatrix} 1 & \frac{1}{\epsilon} & \frac{1}{\epsilon^2} & \frac{1}{\epsilon^3} & . & . \\ 0 & 0 & 0 & 0 & . & . \\ 0 & 0 & 0 & 0 & . & . \\ . & . & . & . & . & . \\ . & . & . & . & . & . \end{pmatrix},$$

$$D_I = \begin{pmatrix} d_I^{1,1} & d_I^{1,2} & d_I^{1,3} & d_I^{1,4} & . & . \\ 0 & d_I^{2,2} & d_I^{2,3} & d_I^{2,4} & . & . \\ 0 & 0 & d_I^{3,3} & d_I^{3,4} & . & . \\ 0 & 0 & 0 & d_I^{4,4} & . & . \\ . & . & & & . & \\ . & . & & & & . \end{pmatrix}, \quad I = 1, 2,$$

$$d_I^{m,m+r} = \frac{(m)_r}{r!\, p_I^r}\left(\frac{q_I}{p_I}\right)^{m-1} d_I^{1,1}, \quad \forall r \geqslant 0,$$

$$d_1^{1,1} = w_{21}, \quad d_2^{1,1} = w_{12}. \tag{9}$$

The notation $(m)_r$ corresponds to Pochhammer symbol for rising factorials, $(m)_r := m(m+1)(m+2)\ldots(m+r-1)$. In Eq. (9), the matrices D_1 and D_2, representing the two nonconserved species, are upper triangular matrices, whose elements involve their corresponding hop rates and the flip rate from the other species (e.g., D_1 involves p_1, q_1, w_{21}). The impurity is represented by the matrix A which has nonzero elements in the first row only, the elements being functions of the impurity hop rate ϵ. The matrix E, characterizing vacancy, is a lower shift matrix.

We should mention that the matrix representations for any number of nonconserved species μ ($\mu = 2$ for the present discussion), i.e., μ-ASEP-IAF, has been obtained recently in Ref. [76]. However, we emphasize that the exact analytical calculations of observables and their properties strongly depend on the choice of initial configurations, owing to the nonergodicity resulting from the microscopic dynamics Eq. (1). Particularly, the initial configuration considered in Ref. [76] is only a special case of the one that would be discussed in the next section (Sec. IV). In fact, interestingly, as we would show later, the onset of clustering and its demarcation from the free-flowing phase, crucially depend on the choice of initial configuration (Sec. VI).

IV. INITIAL CONFIGURATION AND PARTITION FUNCTION

In spite of the presence of flip-dynamics, the microscopic dynamics in Eq. (1) preserves certain orderings of the different species and impurities from initial configuration. It implies that the system is nonergodic and can access only a subspace of the whole configuration space, starting from a particular initial configuration. To demonstrate the cluster formation in 2-ASEP-IAF, we consider the following initial configuration (represented by corresponding matrices),

$$D_2A \ldots D_2A\ D_1A \ldots D_1A\ D_1 \ldots D_1\ E \ldots E. \tag{10}$$

The dots in $\mathcal{Y}\ldots\mathcal{Y}$ ($\mathcal{Y} = D_2A, D_1A, D_1$ and E) represent an uninterrupted sequence of the unit $\mathcal{Y}$. Note that, there are two types of species 1 particles in Eq. (10). One type is those which can flip, belongs to the sequence $\mathcal{Y} = D_1A$, while the others are nonflipping species 1 particles belonging to the sequence $\mathcal{Y} = D_1$. The density of such nonflipping species 1 particles is denoted by

$$\bar{\rho} := \frac{\bar{N}}{L}, \tag{11}$$

where the number of particles of species 1 that cannot flip to species 2 is given by $\bar{N}$. We do not require to introduce such symbol for species 2 since the number of nonflipping species 2 particles is zero in Eq. (10). A careful look at the initial configuration [Eq. (10)] and the dynamics [Eq. (1)] reveals that each configuration in the system can be identified as a sequence of intervals between impurities. Each interval contains one species 1 or species 2 particle and vacancies, except one interval that contains additional $\bar{N}$ nonflipping species 1 particles apart from the one particle that can flip. The species 1 and species 2 particles can hop to right or left within this interval and can flip into each other at the two boundaries (i.e., impurities) of the interval. Each interval can increase or decrease in size by the incoming or outgoing vacancies at the right and left interval boundaries, respectively. This effectively gives rise to a cyclic motion of the intervals toward right.

For convenience, we calculate the partition function corresponding to the initial configuration Eq. (10) in the grand canonical ensemble, by associating the fugacity z_0 with the vacancies (0). Consequently, the partition function would be

$$Q = \sum_{m_1=0}^{\infty} \cdots \sum_{m_{N_+}=0}^{\infty} \sum_{\tilde{m}_1=0}^{\infty} \cdots \sum_{\tilde{m}_{N_+}=0}^{\infty} \sum_{n_1=0}^{\infty} \cdots \sum_{n_{\bar{N}}=0}^{\infty} \mathrm{Tr} \times \left[\left(\prod_{i=1}^{N_+} (D_1 + D_2)(z_0E)^{m_i} A (z_0E)^{\tilde{m}_i} \right) \times \left(\prod_{j=1}^{\bar{N}} D_1 (z_0E)^{n_j} \right) \right]. \tag{12}$$

The emergence of the products inside the trace in Eq. (12) can be understood from the interpretation of each configuration as a sequence of intervals between impurities discussed above. Since we have N_+ impurities in the periodic system, that leads to N_+ intervals each bounded by impurities at both ends. This corresponds to the product of N_+ intervals in the first term inside the trace in Eq. (12). Each product in the first term inside the trace correspond to interval containing one particle that can flip, whereas the last product term denotes the sequence of $\bar{N}$ nonflipping species 1 particles inside the one exceptional interval. We would use the explicit matrix representations from Eq. (9) to calculate the partition function

in Eq. (12). It is suitable to write down the matrices in the concise form as

$$\begin{aligned} E &= \sum_{\gamma=1}^{\infty} |\gamma+1\rangle\langle\gamma| \Rightarrow E^n = \sum_{\gamma=1}^{\infty} |\gamma+n\rangle\langle\gamma|, \\ D_{1,2} &= \sum_{\alpha=1}^{\infty}\sum_{\beta=\alpha}^{\infty} (d_{1,2})_{\alpha,\beta}|\alpha\rangle\langle\beta|, \\ (d_{1,2})_{\alpha,\beta} &:= \frac{(\beta-1)!}{(\alpha-1)!(\beta-\alpha)!}\frac{q_{1,2}^{\alpha-1}}{p_{1,2}^{\beta-1}}, \\ A &= \sum_{\delta=1}^{\infty} \frac{1}{\epsilon^{\delta-1}}|1\rangle\langle\delta|, \end{aligned} \tag{13}$$

where $\langle k| = (0, 0, \ldots 1, \ldots 0)$ is a standard basis vector with only nonzero element 1 at the kth place and $|k\rangle = (0, 0, \ldots 1, \ldots 0)^T$, where the superscript T denotes transpose of the vector under consideration. With the above expressions, we can simplify the matrix strings in Eq. (12). For example, we obtain

$$\begin{aligned} \prod_{j=1}^{\bar{N}} D_1(z_0E)^{n_j} = \sum_{n_1}\cdots\sum_{n_{\bar{N}}}\sum_{\alpha_1}\sum_{\alpha_2}\cdots\sum_{\alpha_{\bar{N}}}\sum_{\beta_{\bar{N}}} z_0^{n_1+\cdots+n_{\bar{N}}} \\ \times (d_1)_{\alpha_1,\alpha_2+n_1}\ldots(d_1)_{\alpha_{\bar{N}-1},\alpha_{\bar{N}}+n_{\bar{N}-1}} \\ \times (d_1)_{\alpha_{\bar{N}},\beta_{\bar{N}}+n_{\bar{N}}}|\alpha_1\rangle\langle\beta_{\bar{N}}|. \end{aligned} \tag{14}$$

We incorporate the explicit form of $(d_1)_{\alpha,\beta}$ from Eq. (13) to evaluate the sums in Eq. (14). However, it is instructive to perform the above calculation recursively, i.e., first for single D_1, then two D_1, followed by three D_1 and finally generalize the result for $\bar{N}$ D_1-s by noting the trend. However, after invoking Eq. (13), the other string of matrices in Eq. (12) reduces to

$$\begin{aligned} &\prod_{i=1}^{N_+}(D_1+D_2)(z_0E)^{m_i}A(z_0E)^{\bar{m}_i} \\ &= \left\{\sum_{m_1} z_0^{m_1}\sum_{\alpha_1}[(d_1)_{\alpha_1,1+m_1}+(d_2)_{\alpha_1,1+m_1}]|\alpha_1\rangle\right\} \\ &\times\left\{\sum_m\sum_n \frac{z_0^{m+n}}{\epsilon^{n-1}}\sum_\alpha\left[\frac{(d_1)_{\alpha,1+m}}{\epsilon^\alpha}+\frac{(d_2)_{\alpha,1+m}}{\epsilon^\alpha}\right]\right\}^{N_+-1} \\ &\times\sum_{\bar{m}_{N_+}} z_0^{\bar{m}_{N_+}}\sum_{\delta_{N_+}}\frac{\langle\delta_{N_+}|}{\epsilon^{\delta_{N_+}-1+\bar{m}_{N_+}}}. \end{aligned} \tag{15}$$

Using Eqs. (14) and (15) in Eq. (12), along with the explicit forms of $(d_{1,2})_{\alpha,\beta}$ from Eq. (13), we finally arrive at the following expression of the partition function

$$\begin{aligned} Q = \left(\frac{1}{1-\frac{z_0}{\epsilon}}\right)^{N_+}\left[\frac{w_{21}}{1-\frac{z_0}{p_1}-\frac{z_0}{\epsilon}\frac{q_1}{p_1}}+\frac{w_{12}}{1-\frac{z_0}{p_2}-\frac{z_0}{\epsilon}\frac{q_2}{p_2}}\right]^{N_+-1} \\ \times\prod_{k=1}^{\bar{N}}\frac{w_{21}}{1-\frac{z_0}{p_1}S_{k-1}}\times\left[\frac{w_{21}}{1-\frac{z_0}{p_1}S_{\bar{N}}}+\frac{w_{12}}{1-\frac{z_0}{p_2}-\frac{q_2}{p_2}\frac{z_0}{p_1}S_{\bar{N}-1}}\right], \end{aligned} \tag{16}$$

where

$$\begin{aligned} S_k &:= \sum_{j=0}^{k}\left(\frac{q_1}{p_1}\right)^j+\left(\frac{q_1}{p_1}\right)^k\frac{q_1}{\epsilon} \\ &= \frac{p_1\left\{\left(\frac{q_1}{p_1}\right)^{k+1}[(k+1)(p_1-q_1)-\epsilon]+\epsilon\right\}}{(p_1-q_1)\epsilon}. \end{aligned} \tag{17}$$

The fugacity z_0 is computed from the density-fugacity relation

$$\rho_0 = \frac{z_0}{L}\frac{d}{dz_0}\ln Q. \tag{18}$$

Thus, we have obtained the analytical form of the partition function Eq. (17) corresponding to the initial configuration Eq. (10).

V. TWO PHASES: ANALYTICAL RESULTS

In this section, we discuss exact results for observables, showing the emergence of two different phases in the 2-ASEP-IAF, with the variation of the parameter q_1. Starting from the initial configuration Eq. (10), the analytical calculations are performed following the footsteps sketched in the previous section, where we use the explicit representations of the matrices from Eq. (9). Before entering into the detailed discussions of the observables, below we briefly summarize our main findings.

(i) The analytical results for one-point (average species densities), two-point (drift current) and n-point functions (correlation between consecutive vacancies) exhibit the existence of two-different phases: the *free-flowing phase* and the *clustering phase*. In Figs. 1(a) and 1(b), we present the heat maps for average species density and average drift current (for species 1), respectively, in the parameter plane p_1-q_1. Figure 1(b) prominently distinguishes two phases separated by the line $q_1 = p_1$. Figure 1(a) also shows two distinct phases demarcated by a region around the line $q_1 = p_1$.

(ii) The average species density (of species 1), when plotted against q_1, remarkably exhibits two different behaviors for $q_1 < p_1$ and $q_1 > p_1$. For $q_1 < p_1$, defining the free-flowing phase, the density is *nonmonotonic*, whereas it remains *constant* for $q_1 > p_1$ that constitutes the clustering phase. Thus the nonconservation plays an important role in identifying the two different phases through a simple one point function.

(iii) The average drift current (of species 1) is *nonzero* in the free-flowing phase, followed by a sharp descent toward zero near $q_1 = p_1$, and remains vanishingly small in the clustering phase.

(iv) The n-point correlation function between n consecutive vacancies increases with increasing n in the counterflow phase, directly pointing toward the formation of vacancy cluster and consequently that of particle cluster.

A. Average species density

We first consider the one-point functions, i.e., the average species densities $\rho_1 = \langle 1\rangle$ and $\rho_2 = \langle 2\rangle$ of the nonconserved species 1 and 2, respectively, where $\langle . \rangle$ denotes ensemble average in the steady state. Since, the total density of the two species remain constant ($\rho_1 + \rho_2 = \bar{\rho} + \rho_+$), it would be sufficient to focus only on the density behavior of one of the species, say ρ_1. The formal expression for $\langle 1\rangle$ that has been

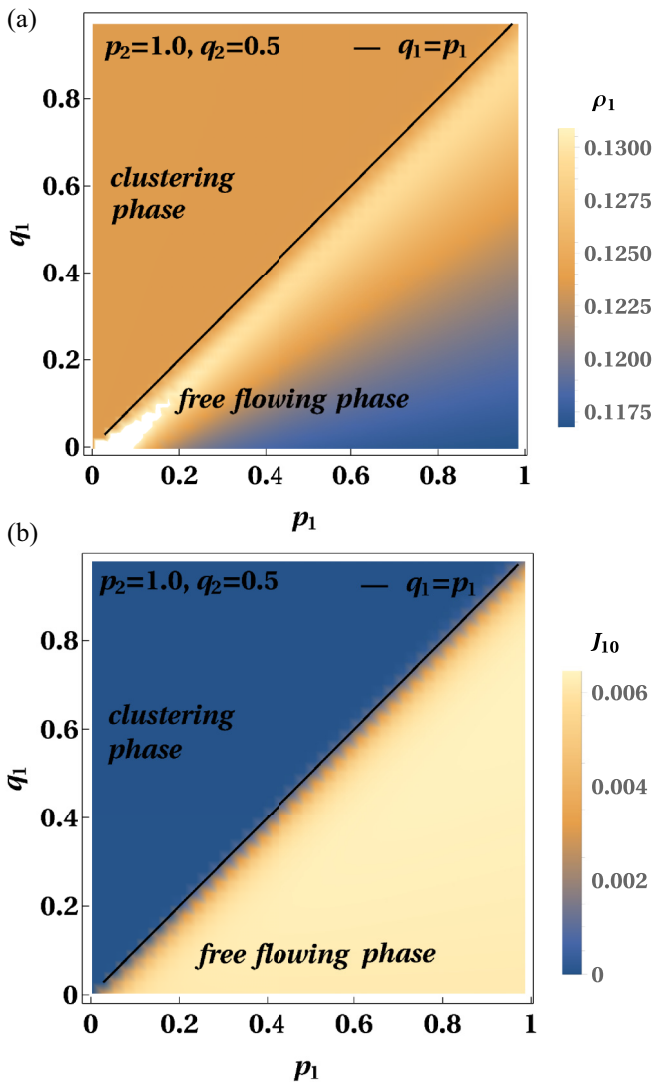

FIG. 1. Panels (a) and (b) show heat-maps for density ρ_1 and current J_{10}, respectively, for species 1, in the p_1-q_1 parameter plane. Both of them, particularly panel (b) clearly exhibits that $q_1 = p_1$ separates two different phases. Panel (a) also implies the nonmonotonicity of the density. The parameters used are $L = 10^3$, $p_2 = 1.0$, $q_2 = 0.5$, $\epsilon = 0.1$, $w_{12} = 1.0$, $w_{21} = 0.1$, $\rho_+ = 0.25$, $\rho_0 = 0.4$.

used to calculate ρ_1, is presented in Eq. (A1) of Appendix A. With the aid of Eqs. (14) and (15), the Eq. (A1) leads to the following exact formula

$$\rho_1 = \bar{\rho} + \left(\rho_+ - \frac{1}{L}\right) \frac{\frac{w_{21}}{1-\frac{z_0}{p_1}S_0}}{\left[\frac{w_{21}}{1-\frac{z_0}{p_1}S_0} + \frac{w_{12}}{1-\frac{z_0}{p_2}(1+\frac{q_2}{p_1}S_{-1})}\right]} + \frac{1}{L}\frac{\frac{w_{21}}{1-\frac{z_0}{p_1}S_{\tilde{N}}}}{\left[\frac{w_{21}}{1-\frac{z_0}{p_1}S_{\tilde{N}}} + \frac{w_{12}}{1-\frac{z_0}{p_2}(1+\frac{q_2}{p_1}S_{\tilde{N}-1})}\right]}, \tag{19}$$

where S_k ($k = 0$ or -1 or N or $N-1$) is given by Eq. (17). To express the density in Eq. (19) as a function of the input parameters only, it is required to solve for z_0, the density-fugacity relation Eq. (18) which more explicitly takes the form Eq. (B1). However, the closed form solution of Eq. (B1) is difficult to obtain. The solution of z_0 obtained from Mathematica, is used to replace it in Eq. (19). We present the corresponding analytical results (solid line) for ρ_1, agreeing with Monte Carlo simulation results (dots) as a function of q_1 in Fig. 2. It is fascinating that even the simplest one-point function, namely the average species density, clearly indicates the existence of two different phases. In one phase, occurring in the parameter region $q_1 < p_1$, the density exhibits a *nonmonotonic* behavior. Whereas it remains *constant* in the other phase, characterizing the parameter region $q_1 > p_1$. As one increases q_1 starting from zero, the hopping of species 1 particles to left, becomes increasingly likely. This means lesser chances for species 1 particles to have impurities as their right nearest neighbors. Consequently, the flipping of species 1 to 2 decreases with increasing q_1, and therefore ρ_1 increases. After reaching the maximum density, ρ_1 starts decreasing, that results in a steep fall near $q_1 \lesssim p_1$. For $q_1 > p_1$, the density remains constant indicating that the drift process no longer can affect ρ_1, meaning the species 1 particles cannot access vacancies due to possible clustering. The point $q_1 = p_1$ demarcating two different phases, is regarded as the transition point. Note that the Fig. 2 is a cross section of Fig. 1(a) at $p_1 = 0.4$, and further clarifies the behavior of ρ_1 observed in the heat-map in Fig. 1(a).

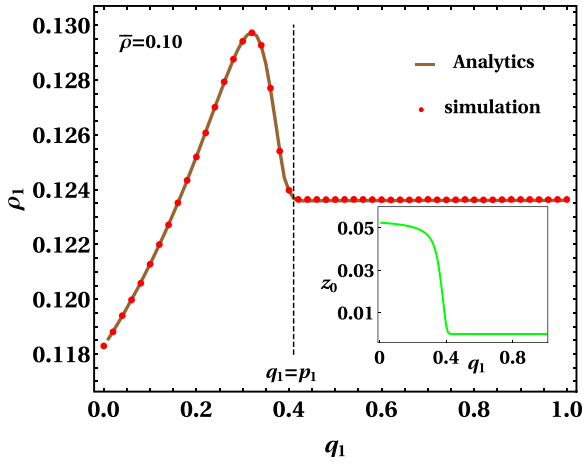

FIG. 2. The figure shows the behavior of the average species density as a function of the counterflow parameter, obtained from analytical result (brown solid line) and Monte Carlo simulation (red dots). Two different phases are apparent, separated by the transition point $q_1 = p_1$. For $q_1 < p_1$, the density exhibits nonmonotonicity whereas for $q_1 > p_1$ the density remains constant. The inset presents the variation of z_0 with q_1. The fugacity exhibits a sharp decrease toward zero in $q_1 \lesssim p_1$ and remains close to zero for $q_1 > p_1$. The parameters used are $L = 10^3$, $p_1 = 0.4$, $p_2 = 1.0$, $q_2 = 0.5$, $\epsilon = 0.1$, $w_{12} = 1.0$, $w_{21} = 0.1$, $\rho_+ = 0.25$, $\rho_0 = 0.4$.

To see how the two different behaviors of ρ_1, nonmonotonic (in $q_1 < p_1$) and constant (in $q_1 > p_1$), are influenced by that of the fugacity z_0, we show the variation of z_0 with q_1 in the inset of Fig. 2. The inset shows that z_0 has a sharp decrease near $q_1 = p_1$ and it is almost zero in the regime $q_1 > p_1$. Consequently, we can take the limit $z_0 \to 0$ in Eq. (19) which would give us the working formula for ρ_1 in the constant density phase. This leads us to the following formula:

$$\rho_1 = \bar{\rho} + \frac{w_{21}}{w_{12}+w_{21}}\rho_+, \quad \text{for } q_1 > p_1. \tag{20}$$

Equation (20) clearly manifests that ρ_1 essentially becomes independent of the parameter q_1 in the regime $q_1 > p_1$. The exact above expression for the average species density can be obtained in a situation where we have two species 1 and 2 along with impurities in a system, but no vacancies, meaning the only dynamics is $1+ \underset{w_{21}}{\overset{w_{12}}{\rightleftharpoons}} 2+$ and there is no drift since there are no vacancies. Such analysis strongly points toward the existence of a single cluster consisting of all the particles accompanied by another cluster consisting of only vacancies in our system in the parameter region $q_1 > p_1$. Consequently, this phase is referred as the *clustering phase*. However, for $q_1 < p_1$, the drift process is significant with flows of particles and vacancies, thereafter named as the *free-flowing phase*. In the free-flowing phase, near the transition point, i.e., $q_1 \lesssim p_1$, we find from Eq. (19) that the fall of ρ_1 toward the constant value [Eq. (20)] takes the form below:

$$\rho_1 \approx \bar{\rho} + \frac{w_{21}}{w_{12}+w_{21}}\rho_+ + z_0 \frac{w_{21}w_{12}}{(w_{12}+w_{21})^2}(A_1+A_2) \quad \text{for } q_1 \lesssim p_1, \tag{21}$$

where $A_1 = (\frac{1}{p_1} + \frac{1}{\varepsilon} - \frac{1}{p_2} - \frac{q_2}{p_2\varepsilon})(\rho_+ - \frac{1}{L})$ and $A_2 = (\frac{1}{p_1} + \frac{1}{\varepsilon})[\bar{\rho}(1-\frac{q_2}{p_2}) + \frac{1}{L}] - \frac{1}{p_2 L}$, we have neglected higher orders of z_0. It is evident from Eq. (21) that the fall of ρ_1 in the regime $q_1 \lesssim p_1$ is linear in z_0 and would depend on how z_0 falls to zero in $q_1 \lesssim p_1$ as a function of $(p_1 - q_1)$.

B. Average drift current

The drift currents for the nonconserved species and the impurity are given by

$$\begin{aligned} J_{10} &= p_1\langle 10\rangle - q_1\langle 01\rangle = z_0\rho_1, \\ J_{20} &= p_2\langle 10\rangle - q_2\langle 01\rangle = z_0\rho_2, \\ J_{+0} &= \epsilon\langle +0\rangle = z_0\rho_+. \end{aligned} \tag{22}$$

The average steady-state densities of the nonconserved species are provided in Eq. (19) whereas the impurity density ρ_+ is a conserved quantity. The fugacity z_0 obeys Eq. (18), more precisely, is the solution of Eq. (B1). The analytical result for J_{10} has been presented as a heat-map in Fig. 1(b) which prominently exhibits the existence of two difference phases, demarcated by the line $q_1 = p_1$. In Fig. 3, we present a cross section of Fig. 1(b) at $p_1 = 0.4$. We observe that the current, starting from nonzero value in the free-flowing phase ($q_1 < p_1$), shows a weak increase. This is due to the increasing density in this parameter regime (Fig. 2). However, the slope of the increase of J_{10} (Fig. 3) is much smaller than that of ρ_1 (Fig. 2), because $J_{10} = z_0\rho_1$ and z_0 decreases with q_1 in the same parameter regime (inset of Fig. 2). After reaching the maximum, J_{10} exhibits a sharp fall near the transition point $q_1 = p_1$, and it remains almost zero (i.e., vanishingly small values) in the clustering phase ($q_1 > p_1$). This observation is consistent with the emergence of the cluster formation for $q_1 > p_1$ corresponding to the approximate situation where the vacancies merely play any role, i.e., the drift process is almost absent. As mentioned in the previous section, this gives rise to two macroscopic clusters, one consisting of all particles and the other made of only vacancies. With the drift becoming negligible in the clustering phase, the density remains constant [Fig. 2, Eq. (20)] and the current stays vanishingly small [Fig. 3]. The species 2 and impurity would have similar characteristics of current, therefore we restrict our investigation to J_{10} only.

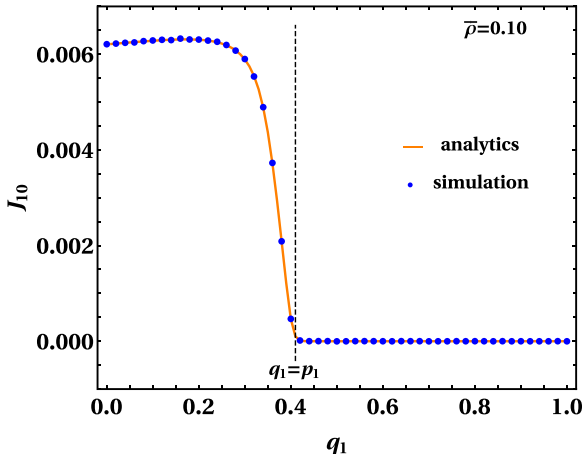

FIG. 3. The figure demonstrates two different phases manifested by the drift current, obtained from analytical result (orange solid line) and Monte Carlo simulation (blue dots). In the parameter regime $q_1 < p_1$, the current is finite whereas it falls abruptly to vanishingly small values at $q_1 = p_1$ and remains so for $q_1 > p_1$. The parameters used are $L = 10^3$, $p_1 = 0.4$, $p_2 = 1.0$, $q_2 = 0.5$, $\epsilon = 0.1$, $w_{12} = 1.0$, $w_{21} = 0.1$, $\rho_+ = 0.25$, $\rho_0 = 0.4$.

From the analysis of the average species density and average current, we understand that the 2-ASEP-IAF can exist in two distinct phases, the free-flowing phase characterized by nonmonotonic density and nonzero current, and the clustering phase identified by constant density and vanishing current. It is important to note that the transition occurs at $q_1 = p_1$ meaning that sufficiently small counterflow is enough to impose clustering in the system.

C. Cluster formation

In Secs. V A and V B, we have inferred the formation of clusters from the features of the density and the current. In this section, we discuss the physical origin of the clustering in 2-ASEP-IAF and provide direct observational evidence of the cluster formation. To analyze the reason behind clustering, we remember that every configuration of the system can be interpreted as a sequence of intervals, as discussed in Sec. IV. Each interval has two impurities at the interval boundaries and particles (species 1 and species 2) that drift within intervals and flip at the boundaries. The total number of particles within each interval is conserved. The intervals can drift toward right and increase or decrease in size as vacancies can enter into and exit from these intervals. The nonflipping species 1 particles inside the rightmost interval presented in Eq. (10), form a dense region against the impurity to their left. This is because the impurity can only move to right as opposed to the nonflipping species 1 sequence that prefers to move left. For each interval, the vacancies can enter the interval *only through right boundary* whereas they can exit from the interval *only through left boundary*. Thus, whichever way the vacancies

are distributed initially within the intervals, at long time they finally exit through the left boundaries of all the intervals and aggregate between the left boundary of leftmost interval and the accumulated species 1 particles in the rightmost interval. Such clustering of vacancies also imply the formation of a cluster of all particles (species 1 and species 2 and impurities). Once the two clusters (particles and vacancies) are formed, the only way for re-entrance of the vacancies inside the particle cluster is by hopping through the accumulated nonflipping species 1 particles. This requires right hopping of these species 1 particles which is less probable as they are left biased. As the sequence of nonflipping species 1 particles becomes larger, it takes longer time for a vacancy to travel thorough the whole particle cluster. It points toward a slow shift of the particle cluster to right and we expect the velocity of the shift to become smaller with increasing $\bar{\rho}$ [Eq. (11)]. We denote the average velocity of the particle cluster by $v_{\rm cl}$. From the expressions for currents (as product of density and velocity) in Eq. (22), the fugacity z_0 [Eq. (18)] is identified to $v_{\rm cl}$.

Next we show the clustering and the drift of the particle cluster explicitly. After the cluster is formed, we start our observation from any configuration and note the position of the particle cluster (determined by the impurity at the leftmost end of the particle cluster) at $\tau = 0$. In Monte Carlo simulation, we measure the position of the cluster at different τ. After time τ, the cluster should shift by an amount of $v_{\rm cl}\tau$. It would be convenient to consider a frame of reference where the cluster remains stationary. Such stationary cluster frame of reference can be conceived by using the shifted lattice index $j'(\tau) := j - v_{\rm cl}\tau$. To characterize the position of particles and vacancies in any configuration, we consider the following observable in the shifted reference frame:

$$\begin{aligned} C_{j'(\tau)} &= 1 \quad \text{if } s'_j = 1 \text{ or } s'_j = 2 \text{ or } s'_j = +\\ &= 0 \quad \text{if } s'_j = 0. \end{aligned} \tag{23}$$

From the Monte Carlo simulation results in Fig. 4, we observe that two macroscopic clusters are formed in the system at any τ, one consisting of all the particles and the other made up of all the vacancies. Further, the cluster is observed to form at the *same* position in the shifted frame of reference, for different τ. This implies that the cluster indeed moves with velocity $v_{\rm cl}$ in the original frame of reference. The slow shift of the cluster is similar to time crystals [56–60]. Note that the slow shift in our model is caused by the unidirectional motion of impurities, and thus the emergence of this slow shift is not contradictory with the no-go theorem of time crystals [58]. The inset of Fig. 4 shows the variation of $v_{\rm cl}$ as a function of the density $\bar{\rho}$ [Eq. (11)] of the nonflipping species 1 particles. We observe that, with increasing $\bar{\rho}$, the cumulative effect of nonflipping species 1 particles (prone toward left hopping) increases and thereby the cluster velocity (toward right) decreases.

D. Spatial correlation

An illuminating way to analytically show the formation of clusters, is to calculate the n-point correlation between consecutive vacancies (it is more helpful than calculating correlations between particles, because we have mixture of different species and impurities inside the particle cluster). The formal expression for the expression for n-point correlation function between n consecutive vacancies, is the following

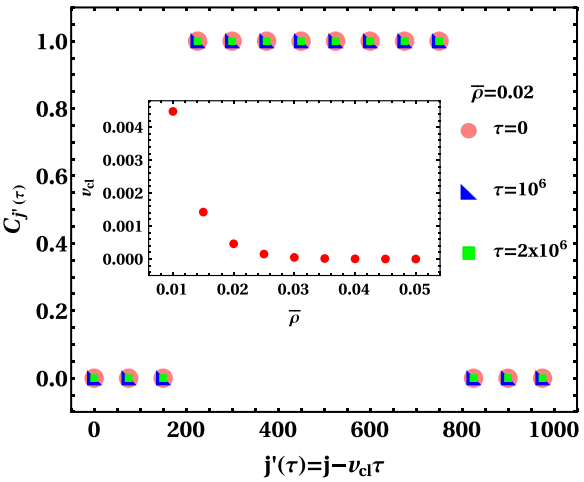

FIG. 4. The figure shows the formation of two macroscopic clusters of particles and vacancies for $q_1 > p_1$, obtained from Monte Carlo simulation. The clusters remain stationary in the shifted reference frame $j' = j - v_{\rm cl}\tau$, implying the drift of cluster with velocity $v_{\rm cl}$ in the original frame of reference. The cluster velocity $v_{\rm cl}$ decreases with increasing $\bar{\rho}$ [Eq. (11)], shown in the inset. The parameters used are $L = 10^3$, $p_1 = 0.4$, $q_1 = 0.5$, $p_2 = 1.0$, $q_2 = 0.5$, $\epsilon = 0.1$, $w_{12} = 1.0$, $w_{21} = 0.1$, $\rho_+ = 0.29$ and $\rho_0 = 1 - 2\rho_+ - \bar{\rho}$.

$$C_0^{[n]} = \langle 00\ldots0\rangle - \langle 0\rangle^n. \tag{24}$$

The superscript $[n]$ in Eq. (24) represents the length of the uninterrupted sequence of consecutive vacancies (denoted by 0 in the subscript). In fact, the above correlation can be obtained recursively starting from the two-point correlation $C_0^{[2]} = \langle 00\rangle - \rho_0^2$. We obtain the following expression for the two point correlation (see Appendix A for more details),

$$\begin{aligned} C_0^{[2]} = \rho_0 - \rho_0^2 - \left(\rho_+ - \frac{1}{L}\right)\frac{z_0}{\epsilon} - \frac{1}{L}\frac{z_0}{p_1}\sum_{k=0}^{\bar{N}-1} S_k \\ - \left(\rho_+ - \frac{1}{L}\right)\frac{\frac{w_{21}X_1}{1-X_1} + \frac{w_{12}X_2}{1-X_2}}{\frac{w_{21}}{1-X_1} + \frac{w_{12}}{1-X_2}} - \frac{1}{L}\frac{\frac{w_{21}Y_1}{1-Y_1} + \frac{w_{12}Y_2}{1-Y_2}}{\frac{w_{21}}{1-Y_1} + \frac{w_{12}}{1-Y_2}}, \end{aligned} \tag{25}$$

where S_k is given by Eq. (17) and $X_1 = \frac{z_0}{p_1} + \frac{z_0}{\epsilon}\frac{q_1}{p_1}$, $X_2 = \frac{z_0}{p_2} + \frac{z_0}{\epsilon}\frac{q_2}{p_2}$, $Y_1 = \frac{z_0}{p_1}S_{\bar{N}}$, $Y_2 = \frac{z_0}{p_2} + \frac{z_0}{p_1}\frac{q_2}{p_2}S_{\bar{N}-1}$. The sum $\frac{1}{L}\sum_{k=0}^{\bar{N}-1} S_k$ in Eq. (25), and consequently $C_0^{[2]}$, can be obtained in closed form, given by Eq. (A8) in Appendix A. We also provide the successive expressions of $C_0^{[n]}$ for different n, along with the corresponding formula for any general n in Eq. (A9) (Appendix A). The variation of $C_0^{[n]}$ with the counterflow parameter q_1 for different values of n, is presented in Fig. 5. For each n the correlation, similar to density and current, displays the existence of two different phases for $q_1 < p_1$ and $q_1 > p_1$. In Fig. 5, we observe a steep increase in the correlations near $q_1 \lesssim p_1$. Interestingly, the correlations between consecutive vacancies increase considerably with increasing n for $q_1 > p_1$.

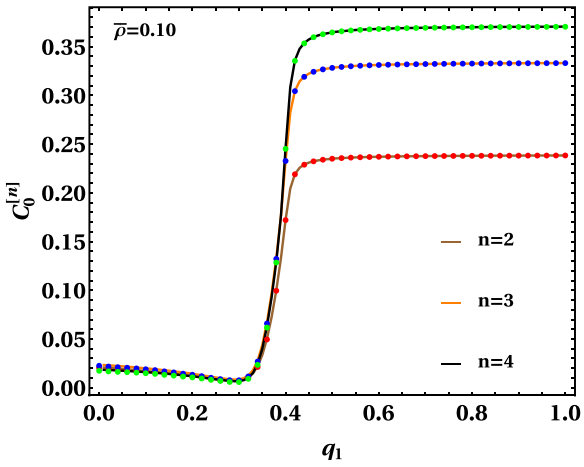

FIG. 5. The figure shows abrupt change in the n-point correlation between consecutive vacancies near the transition point $q_1 = p_1$. For $q_1 > p_1$, the growth of the correlation with increasing n implies the tendency of vacancies to form larger cluster. Solid lines and dots correspond to analytical calculation and Monte Carlo simulation results, respectively. The parameters used are $L = 10^3$, $p_1 = 0.4$, $p_2 = 1.0$, $q_2 = 0.5$, $\epsilon = 0.1$, $w_{12} = 1.0$, $w_{21} = 0.1$, $\rho_+ = 0.25$, $\rho_0 = 0.4$.

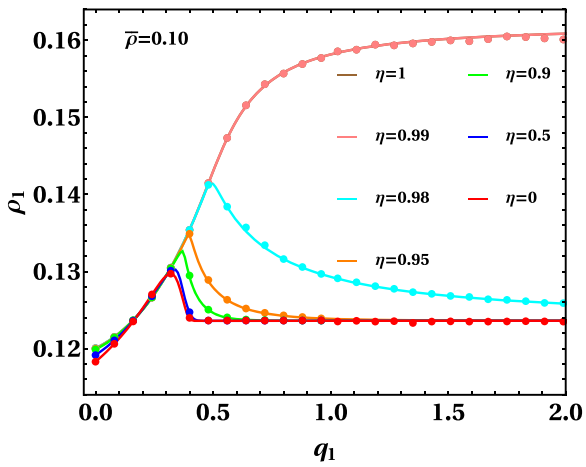

FIG. 6. The figure demonstrates the effect of rearrangement parameter η (characterizing nonergodicity) on the clustering phase. As η decreases, the distinction between the free-flowing phase and clustering phase becomes more and more abrupt. Particularly, the density remains monotonic for large $\eta \approx 1$, whereas it is nonmonotonic for small and moderate values of η. Solid lines and dots correspond to analytical calculation and Monte Carlo simulation results, respectively. The parameters used are $L = 10^3$, $p_1 = 0.4$, $p_2 = 1.0$, $q_2 = 0.5$, $\epsilon = 0.1$, $w_{12} = 1.0$, $w_{21} = 0.1$, $\rho_+ = 0.25$, $\rho_0 = 0.4$.

This implies more number of vacancies prefer to stick together in the parameter regime $q_1 > p_1$. It appears to be a direct evidence of macroscopic cluster formation of vacancies in the clustering phase. We use the fact that z_0 remains almost zero in the clustering phase (inset of Fig. 2), in Eq. (25). This simplifies the expression for $C_0^{[2]}$ considerably in the clustering phase and leads to

$$C_0^{[2]} \approx \rho_0 - \rho_0^2, \quad \text{for } q_1 > p_1. \tag{26}$$

The above result is consistent with $C_0^{[2]}$ being constant for $q_1 > p_1$ in Fig. 5, with the corresponding value agreeing to the same given in Eq. (26). In fact, similar arguments apply for general n, and Eq. (A9) consequently results in the following particularly simple expression for $C_0^{[n]}$ in the clustering phase

$$C_0^{[n]} \approx \rho_0 - \rho_0^n, \quad \text{for } q_1 > p_1. \tag{27}$$

We understand from Eq. (27) that with increasing n, $C_0^{[n]}$ approaches to ρ_0 which is simply the density of the vacancies, and this statement is also evident from Fig. 5.

VI. EFFECT OF NONERGODICITY ON CLUSTERING

The discussion of the two different phases up to now, corresponds to the initial configuration Eq. (10). The features of the free-flowing phase and the clustering phase would remain the same for initial configurations that can be prepared by permuting the positions of vacancies in Eq. (10). But, owing to the nonergodic nature of 2-ASEP-IAF, it is important to ask about the effect of the rearrangement of the two species and impurities in the initial configuration Eq. (10). To answer this, in this section we investigate the effect of nonergodicity on the clustering phenomena. We consider the following variation of the initial configuration Eq. (10):

$$D_2A..D_2A\ D_1D_1A..D_1D_1A\ D_1A..D_1A\ D_1..D_1\ E..E. \tag{28}$$

We emphasize that all the input parameters $(p_{1,2}, \epsilon, w_{12,21}, \rho_0, \rho_+, \bar{\rho})$ are same both for Eqs. (10) and (29). The difference between these two initial configurations lies in the *rearrangement* of the nonflipping species 1 particles. In Eq. (29), we have two types of nonflipping species 1 particles, *isolated* (left D_1 of unit D_1D_1A cannot come in contact with another nonflipping D_1), and *nonisolated* (belongs to sequence $D_1..D_1$). For Eq. (10), we have only the nonisolated type. However, the total density of nonflipping D_1 is $\bar{\rho}$, same for both Eq. (10) and Eq. (29). To quantify their difference, we denote the fraction of isolated nonflipping species 1 particles in Eq. (29) as η. If we denote the densities of isolated and nonisolated types of nonflipping species 1 particles by ρ_{iso} and ρ_{niso}, respectively, then η is given by

$$\eta = \frac{\rho_{\text{iso}}}{\bar{\rho}} = 1 - \frac{\rho_{\text{niso}}}{\bar{\rho}}, \tag{29}$$

where $\bar{\rho}$ is defined through Eq. (11). The initial configuration in Eq. (10) corresponds to $\eta = 0$. Since the variation of η simply rearranges the nonflipping D_1-s in the initial configuration, we denote it as *rearrangement parameter*. Thus η appears as a hallmark of nonergodicity. We present the behavior of average species density ρ_1 as a function of η in Fig. 6, obtained in Eq. (A2) (Appendix A), following similar methods discussed in Sec. IV. With decreasing η, the distinction between two phases become more evident in Fig. 6 and the fall of the density to constant value gets sharper. Intriguingly, for small or moderate values of rearrangement parameter, the density is nonmonotonic, contrary to its monotonic nature for $\eta \approx 1$. Figure 6 thus illustrates that the onset of clustering strongly depends on η, and therefore on the choice of the initial configuration. In reality, often there are restrictions on the tunable range of the tuning parameter. For the variable range of the parameter under consideration (e.g., say $q_1 \in (0, 1)$

for some system), Fig. 6 tells us which initial configurations are more prone to clustering in the steady state and which initial configurations are suitable to avoid such clustering, for a given value of q_1. Taking into consideration the possible mapping of the present model to a narrow two-lane system with counterflow, the analysis of diagrams like Fig. 6 might help in predicting the chances of jamming in the steady state starting from different initial configurations.

VII. ANALYSIS OF THE CASE $q_1 - p_1 = p_2 - q_2$: MAPPING TO RUN-AND-TUMBLE PARTICLES

In this section, we consider the subspace of the parameter space that satisfies the constraint $q_1 - p_1 = p_2 - q_2$. This special case is worthy of some detailed analysis because of its underlying connection to run-and-tumble particles.

Self-propelled objects such as bacteria respond to chemical stimulus (e.g., nutrients or harmful substances) present in the environment through the process of *chemotaxis*. Chemotaxis, in a simple language, can be understood as run-and-tumble motion. *Run* corresponds to motion along fixed direction and *tumble* corresponds to intermediate random reorientation of direction of motion. Individual swimming flagellated bacteria, e.g., *Escherichia coli* in suspensions exhibit run-and-tumble dynamics [62,77–79]. More interestingly, there are run-and-tumble wild bacteria, e.g., *Vibrio ordalli* in oceans, for which even the chemical stimulus can be dynamic [63]. The creation, destruction and diffusion of the short-lived chemical stimulus in ocean create the dynamic chemical gradient [63]. Bacteria like *E. coli* or *V. ordalli* can accumulate near chemical stimulus to create clusters [62,63,77]. Such run-and-tumble motion and clustering of bacteria can be best described in two-dimensional continuous space, which poses difficulties for exact analysis. Rather, one-dimensional discrete lattice models, although simpler adaptation of the complex bacterial systems, can capture the run-and-tumble dynamics and cluster formation. In this connection, it is intriguing to note that the 2-ASEP-IAF [Eq. (1)] can be mapped to a system of many RTPs, under the special circumstance $q_1 - p_1 = p_2 - q_2$.

In this case, the net bias of the two species are equal and opposite to each other, and therefore the two species can be considered as the manifestations of two possible orientations of RTPs in one dimension. The impurities act as origins of the tumbling process. The flip between species can be interpreted as tumbling of directions. Particularly, when the impurity causes flip to a species that has net bias in the direction same as that of the impurities, the impurity at that instant can be thought of a attracting reagent or nutrients. However, when the resulting species from flip has net bias opposite to the impurity bias, the impurity at that instant is considered as a repelling reagent for tumbling process. Note that apart from the RTPs [constituted by the D_1-s and D_2-s in the sequences of $\mathcal{Y} = D_1A, D_2A$ in Eq. (10)] and sources of tumbling process [i.e., impurities A in the sequences of $\mathcal{Y} = D_1A, D_2A$ in Eq. (10)], there are particles which do not tumble in the sense that their direction of net bias remain unchanged [the nonflipping D_1-s in the sequence of $\mathcal{Y} = D_1$ in Eq. (10)]. With this mapping of the 2-ASEP-IAF to RTPs, we discuss the behaviors of the average density [Eq. (19)] and current [Eq. (22)] of the species

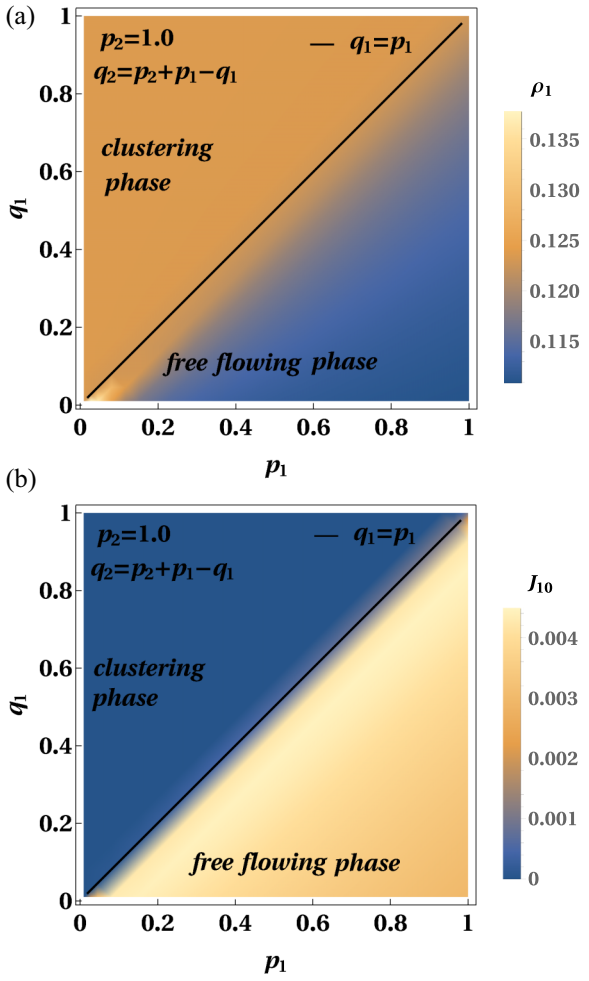

FIG. 7. Panels (a) and (b) show heat-maps for density ρ_1 and current J_{10}, respectively, in the p_1-q_1 plane, for the special case $q_2 - p_2 = p_1 - q_1$ that maps the 2-ASEP-IAF to a system of RTPs. Both figures exhibit the existence of two different phases for $q_1 > p_1$ and $q_1 < p_1$. The current being close to zero for $q_1 > p_1$ in panel (b) confirms that this parameter region corresponds to the clustering phase, while $q_1 < p_1$ with nonzero current gives the free-flowing phase. The parameters used are $L = 10^3$, $p_2 = 1.0$, $\epsilon = 0.1$, $w_{12} = 1.0$, $w_{21} = 0.1$, $\rho_+ = 0.25$, $\rho_0 = 0.4$.

for the special case $q_1 - p_1 = p_2 - q_2$, as a function of the system parameters.

We present the heat-maps of the average density ρ_1 and current J_{10} in Figs. 7(a) and 7(b), in the p_1-q_1 plane. It should be mentioned that the mapping discussed in this section forces us to consider $q_2 - p_2 = p_1 - q_1$, i.e., Fig. 7 strictly corresponds to the counterflow situation (both for $q_1 < p_1$ and $q_1 > p_1$). This is contrary to the setup in Fig. 1 where we have natural flow for $q_1 < p_1$ and counterflow for $q_1 > p_1$. In spite of this, we observe from Fig. 7 that, even within the counterflow scenario, two different phases emerge showing distinct features for $q_1 < p_1$ and $q_1 > p_1$ that are qualitatively similar to Fig. 1. For further analysis, in Figs. 8(a) and 8(b), we present cross sections of Figs. 7(a) and 7(b), respectively, at fixed p_1. Both Figs. 8(a) and 8(b) exhibit two different phases, the free-flowing phase and the clustering phase. For $q_1 < p_1$ and $q_2 > p_2$, both the density and current vary nonmonoton-

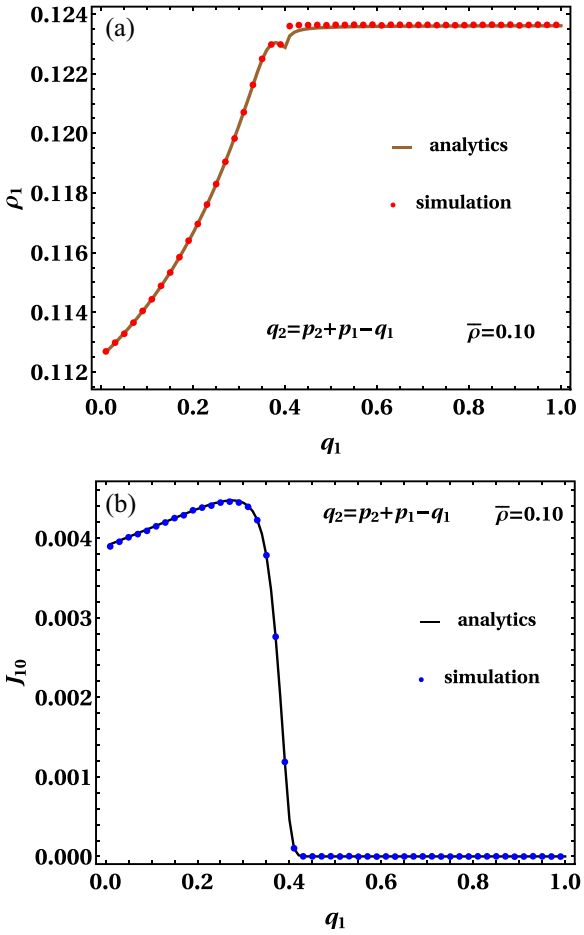

FIG. 8. Panels (a) and (b) show two different phases for the RTPs, through the variation of average species density ρ_1 and average drift current J_{10}, respectively, as functions of the parameter q_1. For $q_1 > p_1$ and $q_2 < p_2$, ρ_1 is constant and J_{10} is vanishingly small, characterizing the phase as clustering phase. For $q_1 < p_1$ and $q_2 > p_2$, we observe the free-flowing phase where both density and current vary considerably with q_1. The solid lines and the dots correspond to analytical and Monte Carlo simulation results, respectively. The parameters used are $L = 10^3$, $p_1 = 0.4$, $p_2 = 1.0$, $\epsilon = 0.1$, $w_{12} = 1.0$, $w_{21} = 0.1$, $\rho_+ = 0.25$, $\rho_0 = 0.4$.

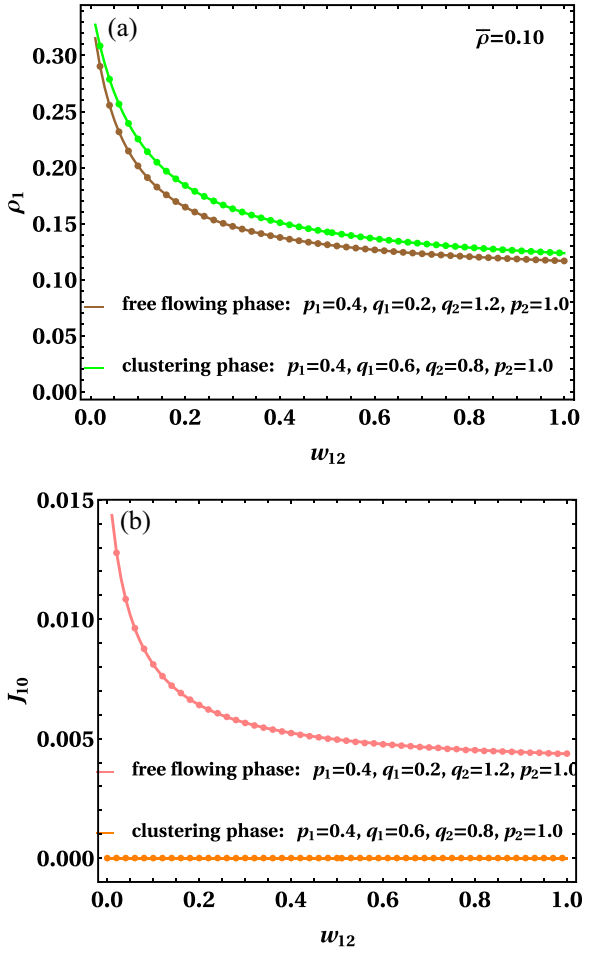

FIG. 9. Panels (a) and (b) illustrate the effect of the tumbling rate w_{12} on the two phases. Panel (a) exhibits similar qualitative behavior (monotonic decrease) of the density ρ_1 in both phases. Panel (b) shows that the clustering phase remains unaffected with the change of w_{12}, whereas the current decreases monotonically with w_{12} in the free-flowing phase. The solid lines and the dots correspond to analytical and Monte Carlo simulation results, respectively. The parameters used are $L = 10^3$, $\epsilon = 0.1$, $w_{21} = 0.1$, $\rho_+ = 0.25$, $\rho_0 = 0.4$.

ically with q_1, which we understand to be the free-flowing phase. Whereas, for $q_1 > p_1$ and $q_2 < p_2$, both ρ_1 and J_{10} remain constant, specifically the current is vanishingly small identifying the phase as the clustering phase. In comparison to Fig. 2 where ρ_1 attains maximum value in the free-flowing phase, the maximum density for Fig. 8(a) is achieved in the clustering phase. The cluster formation owes to the cumulative effect emerging from the presence of the nontumbling sequence of $\mathcal{Y} = D_1$ in the initial configuration Eq. (10). We should mention that there is disagreement to some extent between our exact results and the Monte Carlo simulation results near $q_1 = p_1$ in the clustering phase observed in Fig. 8(a), whereas both results match well for all other values of q_1. This discrepancy, as per our current understanding, is due to the restriction of insufficient ensemble average near the transition point.

It is quite natural to ask the effect of tumbling rates (w_{12} and w_{21}) on the two phases. To investigate this, we present the variation of ρ_1 and J_{10} as functions of the tumbling rate w_{12} in Figs. 9(a) and 9(b), respectively, using our analytical findings (solid lines) from Eqs. (19) and (22), supported by Monte Carlo simulation results (dots). In each figure, we consider two situations, one corresponding to $q_1 < p_1$ and $q_2 > p_2$, and the other to $q_1 > p_1$ and $q_2 < p_2$. Particularly, Fig. 9(b) clearly shows the current remains vanishingly small for any value of w_{12}, in the case $q_1 > p_1$ and $q_2 < p_2$, suggesting that the formed cluster is stable to change of the tumbling rates. However, for $q_1 < p_1$ and $q_2 > p_2$, the current of species 1 decreases monotonically with increasing tumbling rate w_{12} (species 1 to species 2) as expected. However, the fact that the change of tumbling rate does not have any effect on the formed clusters, is not visible from the density characteristics in Fig. 9(a) which shows similar qualitative nature for both the free-flowing and clustering phase. We would also like to

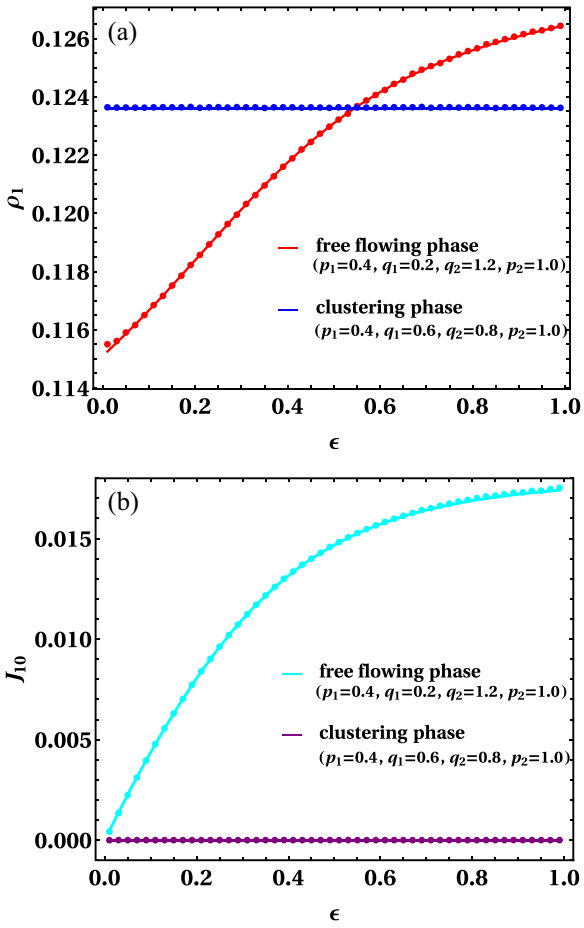

FIG. 10. Panels (a) and (b) illustrate the effect of the drift ϵ of tumbling reagents (i.e., impurities) on the two phases. Both the density and current, in panels (a) and (b), respectively, show that the variation of ϵ has no effect in the clustering phase, whereas both the observables increase monotonically with ϵ in the free-flowing phase. The solid lines and the dots correspond to analytical and Monte Carlo simulation results, respectively. The parameters used are $L = 10^3$, $w_{12} = 1.0$, $w_{21} = 0.1$, $\rho_+ = 0.25$, $\rho_0 = 0.4$.

explore the effect of the drift process of the impurities, that act as attracting reagent (nutrient) or repelling reagent causing the tumbles, on the two phases. The observables ρ_1 and J_{10} in Figs. 10(a) and 10(b), respectively, exhibit that the clustering phase is undisturbed by the change of the impurity drift rate ϵ, where as both the average density and current increases with increasing ϵ in the free-flowing phase. Thus, we have shown that, starting from initial configuration Eq. (10), the system of RTPs (along with attracting or repelling reagents causing tumbles) can transit between free-flowing phase and clustering phase, with the variation of the control parameter q_1 that tunes the net biases of the two tumbling directions. Interestingly, the formed clusters are stable against any change of the tumbling rates w_{12} (and w_{21}) and reagent (i.e., impurity causing tumble) drift rate ϵ.

VIII. SUMMARY

We have demonstrated the formation of clusters induced by counterflow in a nonergodic system. To illustrate this, we have considered two species asymmetric simple exclusion process along with impurities. Apart from the drift of the species and impurities, additionally the impurities activate flips between the two species. The exact analytical results obtained for the observables (average species density, drift current, spatial correlation), show two distinct phases, *free-flowing phase* and *clustering phase*, as functions of the counterflow parameter q_1, which basically controls the flow direction of species 1 by tuning its net bias. The *free-flowing phase* is specified by *nonmonotonic density* and *nonmonotonic finite current*, whereas the *clustering phase* is characterized by *constant density* and *vanishing current*. The clustering situation can be thought as an equivalent system almost devoid of vacancies, where the drift dynamics is *almost* absent. This is compatible with the vanishing current and the constant density in the clustering phase. Specifically, the growth of n-point spatial correlation between n consecutive vacancies with increasing n, directly implies the accumulation of vacancies to form one macroscopic cluster, along with another macroscopic cluster formed by all the particles. The heat maps of density and current in p_1-q_1 plane show that the two phases are demarcated by the line $q_1 = p_1$ (p_1 and q_1 being right and left hop rates of species 1, respectively). This is further clarified by the sharp descents of density and current and the sharp ascent in spatial correlation between vacancies near $q_1 = p_1$. The slow drift of the cluster in the clustering phase can be observed by tracking individual configurations over long time. The effect of nonergodicity on the system is characterized through a rearrangement parameter, which only permutes the positions of some particles while keeping all the input parameters fixed. We observe that the choice of initial configuration affects the onset of clustering significantly. In fact, for certain initial configurations, we do not see signatures of clustering for finite values of q_1 and the corresponding densities increase monotonically in contrast to the nonmonotonic densities for initial configurations showing cluster formations. Interestingly, for a special case of the microscopic dynamics when the net bias of the two species are equal and opposite to each other, we map the 2-ASEP-IAF to a system of RTPs. The species with net bias to right (left) can be considered as right (left) running RTPs, where the impurities act as tumbling reagents that cause the tumbling of RTPs, equivalent to the flip process in 2-ASEP-IAF. Notably, although this mapping is valid only in the counterflow situation, we still observe two different phases, the free-flowing phase and the clustering phase. We further find that the clustering phase remains stable against the variation of the tumbling rate and drift of the tumbling reagents. We believe that our analysis supported by exact analytical results enlightens the understanding of clustering phenomena.

The model studied here, having resemblance to two-lane traffics and RTPs in active matter, points toward analytical understanding of traffic jams and clustering active matter systems. Further careful and thorough investigations are required to establish such connections. It would be interesting to study variations of the local microscopic dynamics considered here, that can produce dynamical ways to get rid of the clustering phase. It would be important to explore the effects of boundary conditions, e.g., allowing entries and exits of

selective particles or all particles, on the different phases of the system.

ACKNOWLEDGMENTS

This work is partially supported by the Grants-in-Aid for Scientific Research (JSPS KAKENHI Grant No. JP21H01006). A.K.C. gratefully acknowledges postdoctoral fellowship from the YITP. The numerical calculations have been done on the cluster Yukawa-21 at the YITP.

APPENDIX A: DERIVATION OF OBSERVABLES

In this Appendix, we sketch the steps for calculating the average species densities and n-point correlation function between consecutive vacancies. These steps essentially follow the methods discussed in obtaining the partition function in Sec. IV. The average density ρ_1 of species 1, can be written as

$$\rho_1 = \langle 1 \rangle = \bar{\rho} + \frac{\left(\rho_+ - \frac{1}{L}\right)}{Q} \sum_{m_1=0}^{\infty} \cdots \sum_{n_{\bar{N}}=0}^{\infty} \mathrm{Tr}\left[D_1 (z_0 E)^{m_1} A (z_0 E)^{\bar{m}_1} \prod_{i=2}^{N_+} (D_1 + D_2)(z_0 E)^{m_i} A (z_0 E)^{\bar{m}_i} \prod_{j=1}^{\bar{N}} D_1 (z_0 E)^{n_j} \right]$$
$$+ \frac{1}{L}\frac{1}{Q} \sum_{m_1=0}^{\infty} \cdots \sum_{n_{\bar{N}}=0}^{\infty} \mathrm{Tr}\left[\prod_{i=1}^{N_+ - 1} (D_1 + D_2)(z_0 E)^{m_i} A (z_0 E)^{\bar{m}_i} \; D_1 (z_0 E)^{m_{N_+}} A (z_0 E)^{\bar{m}_{N_+}} \prod_{j=1}^{\bar{N}} D_1 (z_0 E)^{n_j} \right]. \tag{A1}$$

The term $\bar{\rho}$ appears directly due to the initial density $\bar{\rho}$ of the nonflipping species 1 particles. In the second part with prefactor $(\rho_+ - \frac{1}{L})$, we place at least one D_1 in a flipping term, whereas any other flipping term can have D_1 or D_2; the density of such terms is $(\rho_+ - \frac{1}{L})$. The last part contributes due to the D_1 that is placed in the last flipping term after which the nonflipping D_1-s start. To proceed, we would use the explicit matrix representations in Eq. (9) and the expressions derived in Eqs. (14) and (15) to evaluate the matrix strings in Eq. (A1). This leads us to the final formula for the average species density in Eq. (19). We can follow similar procedure to calculate the average species densities for the general initial configuration Eq. (29) with nonzero η in Sec. VI. In this case, we get

$$\rho_1(\eta) = \bar{\rho} + \left(\rho_+ - \frac{1}{L} - \eta\bar{\rho}\right) \frac{\frac{w_{21}}{1-\frac{z_0}{p_1}S_0}}{\left[\frac{w_{21}}{1-\frac{z_0}{p_1}S_0} + \frac{w_{12}}{1-\frac{z_0}{p_2}(1+\frac{q_2}{p_1}S_{-1})}\right]} + \eta\bar{\rho} \frac{\frac{w_{21}}{1-\frac{z_0}{p_1}S_1}}{\left[\frac{w_{21}}{1-\frac{z_0}{p_1}S_1} + \frac{w_{12}}{1-\frac{z_0}{p_2}(1+\frac{q_2}{p_1}S_0)}\right]}$$
$$+ \frac{1}{L} \frac{\frac{w_{21}}{1-\frac{z_0}{p_1}S_{(1-\eta)\bar{N}}}}{\left[\frac{w_{21}}{1-\frac{z_0}{p_1}S_{(1-\eta)\bar{N}}} + \frac{w_{12}}{1-\frac{z_0}{p_2}(1+\frac{q_2}{p_1}S_{(1-\eta)\bar{N}-1})}\right]},$$
$$\rho_2(\eta) = \bar{\rho} + \rho_+ - \rho_1(\eta), \tag{A2}$$

It is straightforward to check that $\eta = 0$ in Eq. (A2) gives the density in Eq. (19).

The formal expression for two-point nearest neighbor correlation between vacancies is

$$C_0^{[2]} = \langle 00 \rangle - \rho_0^2. \tag{A3}$$

It is difficult to calculate $\langle 00 \rangle$ directly using the matrix representations, rather it is easier to use the following conservation:

$$\langle 00 \rangle + \langle 01 \rangle + \langle 02 \rangle + \langle 0+ \rangle = \rho_0. \tag{A4}$$

Using Eq. (A4) into Eq. (A3), we get

$$C_0^{[2]} = \rho_0 - \rho_0^2 - \langle 01 \rangle - \langle 02 \rangle - \langle 0+ \rangle. \tag{A5}$$

Evaluating $\langle 01 \rangle$, $\langle 02 \rangle$, and $\langle 0+ \rangle$ using the matrix representations, we finally obtain the following expression for C_{00}:

$$C_0^{[2]} = \rho_0 - \rho_0^2 - \left(\rho_+ - \frac{1}{L}\right)\frac{z_0}{\epsilon} - \frac{1}{L}\frac{z_0}{p_1}\sum_{k=0}^{\bar{N}-1} S_k$$
$$- \left(\rho_+ - \frac{1}{L}\right) \frac{\frac{w_{21}X_1}{1-X_1} + \frac{w_{12}X_2}{1-X_2}}{\frac{w_{21}}{1-X_1} + \frac{w_{12}}{1-X_2}} - \frac{1}{L} \frac{\frac{w_{21}Y_1}{1-Y_1} + \frac{w_{12}Y_2}{1-Y_2}}{\frac{w_{21}}{1-Y_1} + \frac{w_{12}}{1-Y_2}}, \tag{A6}$$

where

$$X_1 = \frac{z_0}{p_1} + \frac{z_0}{\epsilon}\frac{q_1}{p_1},$$
$$X_2 = \frac{z_0}{p_2} + \frac{z_0}{\epsilon}\frac{q_2}{p_2},$$
$$Y_1 = \frac{z_0}{p_1} S_{\bar{N}},$$
$$Y_2 = \frac{z_0}{p_2} + \frac{z_0}{p_1}\frac{q_2}{p_2} S_{\bar{N}-1}. \tag{A7}$$

Clearly, the two-point correlation would have a closed form if the sum $\sum_{k=0}^{\bar{N}-1} S_k$ has a closed form, and indeed this can be evaluated as

$$\frac{1}{L}\sum_{k=0}^{\bar{N}-1} S_k = \bar{\rho}\frac{p_1}{(p_1-q_1)} + \frac{1}{L}\left[1-\left(\frac{q_1}{p_1}\right)^{\bar{N}}\right] \times \left(\frac{p_1-q_1}{\epsilon}-1\right)\frac{p_1 q_1}{(p_1-q_1)^2}. \tag{A8}$$

So, we have evaluated the two-point correlation function $C_0^{[2]}$ exactly. Of course, z_0 has to be calculated from the density-fugacity relation. Importantly in Eq. (A8), note that we could scale $\bar{N}$ by system-size L properly in the first term so that it becomes a function of $\bar{\rho}$, but this is not possible in the case of the second term where $\bar{N}$ appears in the power.

In fact, using the result of $C_0^{[2]}$, we can calculate $C_0^{[3]}$ and then $C_0^{[4]}$ using $C_0^{[3]}$, and so on. For simplified notations, we denote $C_0^{[n]}$ as the correlation between consecutive n vacancies [Eq. (24)], then we obtain in iterative way,

$$\begin{aligned}
C_0^{[2]} &= \rho_0 - \rho_0^2 - \left(\rho_+ - \frac{1}{L}\right)\frac{z_0}{\epsilon} - \frac{1}{L}\frac{z_0}{p_1}\sum_{k=0}^{\bar{N}-1} S_k - \left(\rho_+ - \frac{1}{L}\right)\frac{\frac{w_{21}X_1}{1-X_1}+\frac{w_{12}X_2}{1-X_2}}{\frac{w_{21}}{1-X_1}+\frac{w_{12}}{1-X_2}} - \frac{1}{L}\frac{\frac{w_{21}Y_1}{1-Y_1}+\frac{w_{12}Y_2}{1-Y_2}}{\frac{w_{21}}{1-Y_1}+\frac{w_{12}}{1-Y_2}},\\
C_0^{[3]} &= C_0^{[2]} + \rho_0^2 - \rho_0^3 - \left(\rho_+ - \frac{1}{L}\right)\left(\frac{z_0}{\epsilon}\right)^2 - \frac{1}{L}\left(\frac{z_0}{p_1}\right)^2\sum_{k=0}^{\bar{N}-1}(S_k)^2 - \left(\rho_+ - \frac{1}{L}\right)\frac{\frac{w_{21}X_1^2}{1-X_1}+\frac{w_{12}X_2^2}{1-X_2}}{\frac{w_{21}}{1-X_1}+\frac{w_{12}}{1-X_2}} - \frac{1}{L}\frac{\frac{w_{21}Y_1^2}{1-Y_1}+\frac{w_{12}Y_2^2}{1-Y_2}}{\frac{w_{21}}{1-Y_1}+\frac{w_{12}}{1-Y_2}},\\
C_0^{[4]} &= C_0^{[3]} + \rho_0^3 - \rho_0^4 - \left(\rho_+ - \frac{1}{L}\right)\left(\frac{z_0}{\epsilon}\right)^3 - \frac{1}{L}\left(\frac{z_0}{p_1}\right)^3\sum_{k=0}^{\bar{N}-1}(S_k)^3 - \left(\rho_+ - \frac{1}{L}\right)\frac{\frac{w_{21}X_1^3}{1-X_1}+\frac{w_{12}X_2^3}{1-X_2}}{\frac{w_{21}}{1-X_1}+\frac{w_{12}}{1-X_2}} - \frac{1}{L}\frac{\frac{w_{21}Y_1^3}{1-Y_1}+\frac{w_{12}Y_2^3}{1-Y_2}}{\frac{w_{21}}{1-Y_1}+\frac{w_{12}}{1-Y_2}},\\
&\ldots = \ldots\\
C_0^{[n]} &= C_0^{[n-1]} + \rho_0^{n-1} - \rho_0^n - \left(\rho_+ - \frac{1}{L}\right)\left(\frac{z_0}{\epsilon}\right)^{n-1} - \frac{1}{L}\left(\frac{z_0}{p_1}\right)^{n-1}\sum_{k=0}^{\bar{N}-1}(S_k)^{n-1}\\
&\quad - \left(\rho_+ - \frac{1}{L}\right)\frac{\frac{w_{21}X_1^{n-1}}{1-X_1}+\frac{w_{12}X_2^{n-1}}{1-X_2}}{\frac{w_{21}}{1-X_1}+\frac{w_{12}}{1-X_2}} - \frac{1}{L}\frac{\frac{w_{21}Y_1^{n-1}}{1-Y_1}+\frac{w_{12}Y_2^{n-1}}{1-Y_2}}{\frac{w_{21}}{1-Y_1}+\frac{w_{12}}{1-Y_2}}.
\end{aligned} \tag{A9}$$

Thus, we have obtained the analytical formulas for average species densities, drift currents, and n-point correlation between consecutive vacancies. The results in Eq. (A9) have been used to present the behavior of the correlations with the variation of the counterflow parameter q_1 in Fig. 5.

APPENDIX B: DENSITY-FUGACITY RELATION: SOLUTION FOR SPECIAL CASES

Here we state the explicit form of the density-fugacity relation, calculated from the partition function in Eq. (16). This relation is used to solve the fugacity z_0 as a function of the input parameters. Consequently, we can replace the corresponding value of z_0 in the expressions of the observables, e.g., in Eqs. (19), (22), and (25), so that they become functions of the input parameters only. The formal expression for the density-fugacity relation is given in Eq. (18). Using Eq. (16) in Eq. (18), we have the following explicit form of the density-fugacity relation to solve:

$$\begin{aligned}
&\frac{\rho_+}{1-\frac{z_0}{\epsilon}} + \frac{z_0\left(\rho_+ - \frac{1}{L}\right)}{w_{21}(1-z_0X_2')+w_{12}(1-z_0X_1')} \times\left[w_{21}X_1'\frac{1-z_0X_2'}{1-z_0X_1'} + w_{12}X_2'\frac{1-z_0X_1'}{1-z_0X_2'}\right]\\
&+ \frac{\frac{z_0}{L}}{w_{21}(1-z_0Y_2')+w_{12}(1-z_0Y_1')} \times\left[w_{21}Y_1'\frac{1-z_0Y_2'}{1-z_0Y_1'} + w_{12}Y_2'\frac{1-z_0Y_1'}{1-z_0Y_2'}\right]\\
&+ \frac{1}{L}\sum_{k=1}^{\bar{N}}\frac{1}{1-\frac{z_0}{p_1}S_{k-1}} = \rho_0 + \rho_+ + \bar{\rho},
\end{aligned} \tag{B1}$$

with $X_{1,2}' = X_{1,2}/z_0$ and $Y_{1,2}' = Y_{1,2}/z_0$, where $X_{1,2}$ and $Y_{1,2}$ follow Eq. (A7), S_k is given by Eq. (17). The reason behind such rescaling by z_0 is simply to express $X_{1,2}'$ and $Y_{1,2}'$ as functions of the input parameters only. In general, we have solved Eq. (B1) in Mathematica to get z_0 for a given set of input parameters. Also note that the complexity of the equation increases with increasing number of nonflipping species 1 particles $\bar{N}$, in terms of the highest degree of z present in the polynomial of z_0 in Eq. (B1). For some special cases with specific choices of the hop-rates, one can obtain closed form solutions for the fugacity z_0.

A particularly simple case corresponds to $\bar{N}=0$. This also implies $Y_1' = X_1'$ and $Y_2' = X_2'$, which can be seen directly from Eq. (A7) with the help of Eq. (17). We further consider the special situation of $X_1' = X_2'$. The density-fugacity relation Eq. (B1) simplifies to

$$\frac{z_0\rho_+X_1'}{1-z_0X_1'} + \frac{\rho_+}{1-\frac{z_0}{\epsilon}} = \rho_0 + \rho_+. \tag{B2}$$

The above equation has the following solution:

$$z_0 = \frac{(\rho_0+\rho_+)(1+\epsilon X_1') + \sqrt{(\rho_0+\rho_+)^2(1+\epsilon X_1')^2 - 4\rho_0\epsilon X_1'(\rho_0+2\rho_+)}}{2(\rho_0+2\rho_+)X_1'}. \tag{B3}$$

To better understand the constraint on the hop rates for which we have got the exact solution Eq. (B3), we explore the situation $X_1' = X_2'$, which basically boils down to

$$\epsilon = \frac{q_2 p_1 - q_1 p_2}{p_2 - p_1}. \tag{B4}$$

The above subspace of hop rates can create both natural flow and counterflow situations and also includes the very special case $p_1 = p_2$ and $q_1 = q_2$. We should mention that, even without the assumption $X_1' = X_2'$, we have a quartic equation in z_0 that can be solved exactly in Mathematica. However, the solution of z_0 in that case is too lengthy to include here.

Another noteworthy point is the fugacity z_0 actually equals to the cluster velocity $v_{\rm cl}$ discussed in the main text (see inset of Fig. 4). This is evident from the current-density relation Eq. (22), which can be considered as $J = v_{\rm cl}\rho$ in the clustering phase. In fact, one can check the inset of Fig. 4 in the main text, obtained from Monte Carlo simulations, can be reproduced by calculating z_0 for the corresponding set of input parameters.

APPENDIX C: A COMMENT REGARDING THE INITIAL CONFIGURATION

We have considered steplike initial configuration [Eq. (10)] in the main text. To elaborate, initially all the particles (both species and impurities) occupy consecutive lattice sites with no vacancy between them. Starting from such steplike initial configuration, in the free-flowing phase, the vacancies get randomly distributed between the particles. On the other hand, in the clustering phase, any steady-state configuration remains steplike, with the particle cluster shifting slowly to right.

Naturally, the question arises if the cluster can be formed from an initial configuration which is not steplike, rather there are vacancies distributed between particles. The answer is *yes*. If we start from a non-step-like initial configuration given below,

$$C(0) = D_2 E^{m_1} A E^{\bar{m}_1} \ldots D_2 E^{m_{N_+/2}} A E^{\bar{m}_{N_+/2}}\ D_1 E^{n_1} A E^{\bar{n}_1} \ldots$$
$$D_1 E^{n_{N_+/2}} A E^{\bar{n}_{N_+/2}}\ D_1 E^{r_1} \ldots D_1 E^{r_{\bar{N}}}, \tag{C1}$$

where the total number of vacancies is

$$\sum_{i=1}^{N_+/2} (m_i + \bar{m}_i + n_i + \bar{n}_i) + \sum_{j=1}^{\bar{N}} r_k = N_0. \tag{C2}$$

Note that the above initial configuration contains the exact same ordering of particles as the one [Eq. (10)] studied in the main text and the total number of vacancies are also the same for both configurations, the only difference being the initial configuration [Eq. (10)] in the main text is steplike, whereas Eq. (C1) is non-step-like. Since the ordering of vacancies actually do not matter, both of these initial configurations lead to the same configuration sub-space in the steady state. Thereby all the characteristics of the system in the steady state remain same for both of these initial configurations. Thus we expect to see the clustering phenomena starting from initial configuration Eq. (C1) just like we did for the one in the main text (see Fig. 4). Indeed, in Fig. 11, we observe that the macroscopic cluster is formed in the steady state, while the initial configuration is non-step-like. So, the only advantageous and satisfactory thing about Eq. (C1), is the fact that the cluster is formed in a dynamic way from non-step-like initial configuration.

APPENDIX D: VARIATION OF OBSERVABLES WITH SYSTEM SIZE L

In this Appendix, we present the behaviors of average species density and drift current as function of q_1, for different system sizes L. Note that, the density ρ_1 should be an intensive quantity independent of L and the steady-state current should also be a constant independent of L. In fact, like the fugacities, e.g., temperature, chemical potential which are independent of system size, the fugacity z_0 should also be a constant independent of system size. Thus, z_0, ρ_1, and J_{10} here must show convergence with increasing L. Indeed, the fugacity obtained from the exact numerical data by solving Eq. (B1), show converging behavior with increasing system size in Fig. 12(a). At the transition point $q_1 = p_1$, we investigate the approach of z_0 toward convergence as a function of L, by fitting the data with the functional form $z_0 = cL^{\alpha}$ in Fig. 12(b). Also, both Figs. 13(a) and 13(b) exhibit convergence of the corresponding behaviors of ρ_1 and J_{10} with increasing system

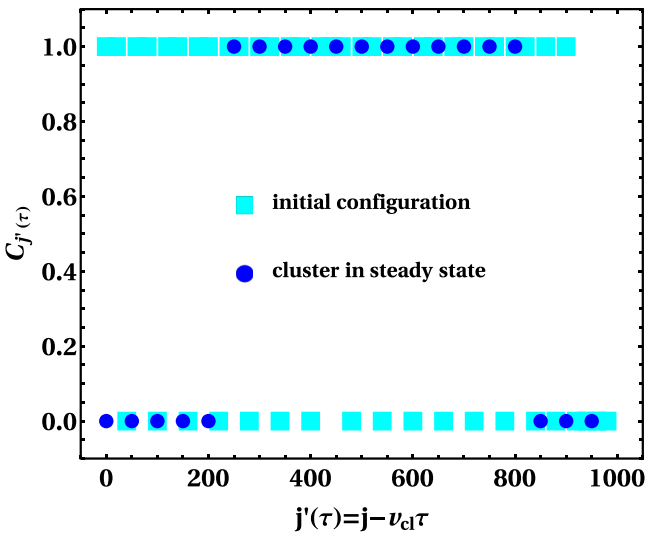

FIG. 11. The figure demonstrates the steplike cluster formation in the steady state, starting from a non-step-like initial configuration where vacancies are randomly distributed among particles. Here we consider $\tau = 0$ as the observation time of cluster in steady state, whereas the initial configuration corresponds to time $t = 0$. The parameters used are $L = 10^3$, $p_1 = 0.4$, $q_1 = 0.5$, $p_2 = 1.0$, $q_2 = 0.5$, $\epsilon = 0.1$, $w_{12} = 1.0$, $w_{21} = 0.1$, $\rho_+ = 0.29$, $\rho_0 = 0.4$.

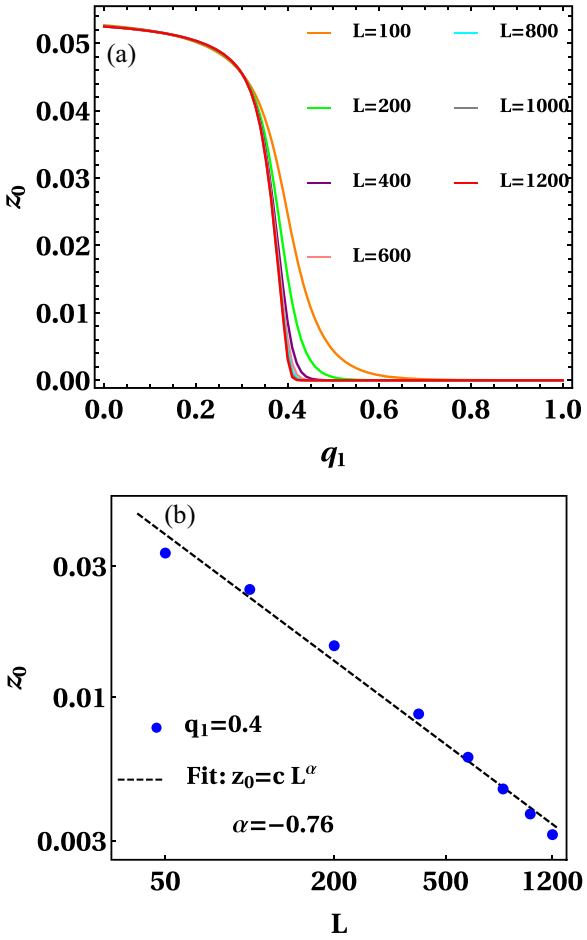

FIG. 12. Panel (a) illustrates the convergence of the fugacity behavior with increasing system size L, plotted against the parameter q_1. Panel (b) illustrates the approach of z_0 toward this convergence with varying L, at the transition point $q_1 = p_1$. The exact numerical data obtained from the solution of z_0 is fitted with the form $z_0 = cL^{\alpha}$, resulting in $\alpha \approx -0.76$. The parameters used are $p_1 = 0.4$, $p_2 = 1.0$, $q_2 = 0.5$, $\epsilon = 0.1$, $w_{12} = 1.0$, $w_{21} = 0.1$, $\rho_+ = 0.25$, $\rho_0 = 0.4$.

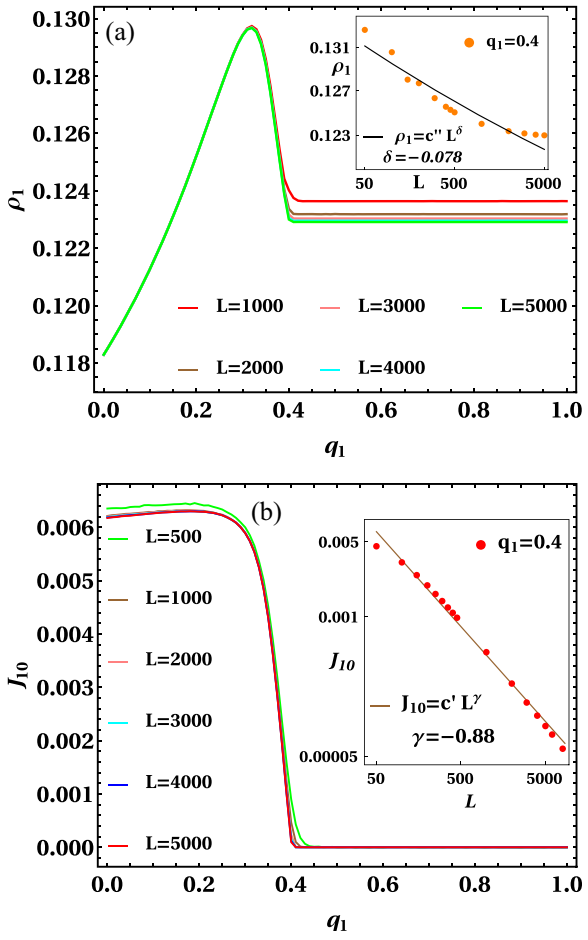

FIG. 13. Panels (a) and (b) show convergence of ρ_1 and J_{10}, respectively, with increasing system size L. The insets (in log scale) of panels (a) and (b) show the variations of ρ_1 and J_{10}, respectively, with L at the transition point $q_1 = p_1$. They follow the relations $\rho_1 = \bar{\rho}c''L^{\delta}$ and $J_{10} = c'L^{\gamma}$ with exponent values $\delta \approx -0.078$ and $\gamma \approx -0.88$ obtained from fitting. The parameters used are $p_1 = 0.4$, $p_2 = 1.0$, $q_2 = 0.5$, $\epsilon = 0.1$, $w_{12} = 1.0$, $w_{21} = 0.1$, $\rho_+ = 0.25$, $\rho_0 = 0.4$.

size. In Fig. 13(b), the current shows rapid convergence in both the free-flowing phase and clustering phase for $L = 10^3$ and more. Notably, in Fig. 13(a), the density shows faster convergence with increasing L in the free-flowing phase, in comparison to that of the clustering phase. We should mention that the convergence value of ρ_1 in the clustering phase in Fig. 13(a) agrees with the simplified formula obtained in Eq. (20). In the insets of Figs. 13(a) and 13(b), we examine the approach of ρ_1 and J_{10}, respectively, toward convergence, with varying system size L. We fit the corresponding data with the relations of the form $\rho_1 = c''L^{\delta}$ and $J_{10} = c'L^{\gamma}$. Keeping in mind the relation [Eq. (22)] between current, density and fugacity of the form $J_{10} = z_0\rho_1$, the exponent δ can be determined from the relation $\delta = (\gamma - \alpha)$. Our findings in Figs. 12 and 13(b) predict δ to be $(\gamma - \alpha) = -0.12$. This is close to but not exactly equal to the δ value ($\approx$−0.078) obtained in the inset of Fig. 13(a) because of the finite system sizes used in the discussion.

APPENDIX E: ARNDT-HEINZEL-RITTENBERG MODEL OF COUNTERFLOW: COMPARISONS

In this section, we compare the microscopic dynamics of our model with the dynamics of the Arndt-Heinzel-Rittenberg (AHR) model that is known to exhibit three different phases [26,80,81]. The AHR model considers positive (say, species 1) and negative (say, species 2) particles along with vacancies (0) on a one-dimensional periodic lattice and the follow the dynamical rules given below

$$10 \xrightarrow{\lambda} 01, \quad 02 \xrightarrow{\lambda} 20, \quad \underset{1}{\overset{q}{\rightleftharpoons}} 21. \tag{E1}$$

A straightforward comparison of the AHR model in Eq. (E1) with our model in Eq. (1) reveal the following factors: (i) our model allows a *nonconserving flip dynamics* that activates transformations between species 1 and 2, which is absent in the AHR model for which each microscopic dynamics maintains particle number conservation of every species. Also, as a consequence, our model requires minimum four species in total (species 1, species 2, impurity and vacancy)

to operate both drift and flip dynamics, while the AHR model deals with three species in total (species 1, species 2, and vacancy). (ii) AHR model has an *exchange dynamics* that allows the two species to exchange their positions. Such exchange dynamics is absent in our case. (iii) Our model is *nonergodic* in contrast to the *ergodic* nature of the AHR model.

The exchange rate q is considered as the tuning parameter for the AHR model and the density ρ of the two species are taken to be equal [26,81]. Three different phases, namely *pure phase*, *mixed phase* and *disordered phase* are observed, as q is varied [26,81]. When $q < 1$, the species 1 is more probable to reside at left of species 2 which again likes to be at left of vacancies. This leads to a complete species segregation with three types of blocks each purely consisting of one species (either 1 or 2 or 0), thereby referred to as pure phase. For $1 < q < q_c$ (where q_c depends on λ and ρ), a condensate is formed that has both species 1 and species 2 mixed up, accompanied by a fluid consisting of vacancies and some particles of the two species. This phase is known as the mixed phase. There is no species segregation or condensate formation for $q > q_c$, which is the disordered phase. To observe these three phases, two point functions like drift current and correlations between different species have been used [26,81].

Interestingly, in our model, due to the presence of nonconserving flip dynamics, we have even simpler one point function like average species densities among observables of interest, and indeed the average species densities clearly show the existence of two different phase, the *free-flowing phase* and the *clustering phase*. The free-flowing phase in our model is similar to the disordered phase of AHR model. However, for the specific choice of initial configuration considered here and due to the flip dynamics, species segregation in *pure* form is not possible in the clustering phase. Rather, we have two macroscopic clusters, one consisting of only vacancies and the other consisting of all kinds of particles (species 1 and species 2 and impurities). Although the mixing up of different species and impurities inside the particle cluster has resemblance to the mixed phase condensate of AHR model, we do not have a background fluid in our case. Rather, for any $q_1 > p_1$, we have only two clusters in the clustering phase, a vacancy cluster and a particle cluster, with the particle cluster drifting along right with considerably small velocity that depends on the density of the nonflipping species 1 particles in the system. Another noteworthy point in our analysis is the *rearrangement parameter* whose variation captures the effect of nonergodicity on the clustering phenomenon, there is no such counterpart in the ergodic AHR model.

Note that exact analysis in Refs. [28,29] later revealed that there is actually no phase transition between mixed and disordered phase in the AHR model, in the thermodynamic limit within the grand canonical ensemble framework. This conclusion is associated with the existence of extremely long but still finite correlation lengths in the infinite system.

There is an alternative approach to compare the dynamics of the two models, although the key points of the comparative analysis between them remain the same. Our tuning parameter has been the counterflow parameter q_1, which is a part of the drift dynamics. To treat the tuning parameter q of the AHR model on an equivalent footing, one can relabel species 1, species 2, and vacancy in AHR model as vacancy, species 1, and species +, respectively. Thus, one arrives at an alternative version of the AHR model given below:

$$0+ \xrightarrow{\lambda} +0, \quad +1 \xrightarrow{\lambda} 1+, \quad 10 \underset{q}{\overset{1}{\rightleftharpoons}} 01. \tag{E2}$$

Here we see, in comparison to our model Eq. (1), the species 2 is absent and we do not term + as impurity because there is no flip dynamics at all. So + drifts to left only, species 1 drifts to right or left with rates q and 1, respectively, with an additional exchange of positions between + and 1. Clearly $q > 1$ here corresponds to natural flow situation and $q < 1$ refers to the counterflow situation.

The exact steady state of AHR model in Eq. (E1) has been obtained in matrix product from, which has a two-dimensional representation in the limit $q \to \infty$ and infinite-dimensional representations in general [81], which have different structures in comparison to the infinite-dimensional matrices in our case Eq. (17).

[1] A. Liu and S. R. Nagel, Nature (London) **396**, 21 (1998).
[2] G. Biroli, Nature Phys. **3**, 222 (2007).
[3] R. P. Behringer and B. Chakraborty, Rep. Prog. Phys. **82**, 012601 (2019).
[4] K. Nagel and M. Schreckenberg, J. Phys. I France **2**, 2221 (1992).
[5] D. Helbing, Rev. Mod. Phys. **73**, 1067 (2001).
[6] T. Nagatani, Rep. Prog. Phys. **65**, 1331 (2002).
[7] A. Schadschneider, D. Chowdury, and K. Nishinari, *Stochastic Transport in Complex System: From Molecules to Vehicles* (Elsevier, Amsterdam, 2011).
[8] R. Mandal, P. J. Bhuyan, P. Chaudhuri, C. Dasgupta, and M. Rao, Nat. Commun. **11**, 2581 (2020).
[9] J. Yang, R. Ni, and M. P. Ciamarra, Phys. Rev. E **106**, L012601 (2022).
[10] M. Sadati, N. T. Quazvini, R. Krishnan, C. Y. Park, and J. J. Fredberg, Differentiation **86**, 121 (2013).
[11] L. Oswald, S. Grosser, D. M. Smith, and J. A. Käs, J. Phys. D: Appl. Phys. **50**, 483001 (2017).
[12] V. Trappe, V. Prasad, L. Cipelletti, P. N. Segre, and D. A. Weitz, Nature (London) **411**, 772 (2001).
[13] M. Muramatsu, T. Irie, and T. Nagatani, Physica A **267**, 487 (1999).
[14] Y. Tajima, K. Takimoto, and T. Nagatani, Physica A **313**, 709 (2002).
[15] D. Helbing and P. Molnár, Phys. Rev. E **51**, 4282 (1995).
[16] *Traffic and Granular Flow '03*, edited by S. P. Hoogendoorn, S. Luding, P. H. L. Bovy, M. Schreckenberg, and D. E. Wolf (Springer, Berlin/Heidelberg/New York, 2005).
[17] T. Kretz, M. Wölki, and M. Schreckenberg, J. Stat. Mech. (2006) P02005.
[18] *Pedestrian and Evacuation Dynamics 2008*, edited by W. W. F. Klingsch, C. Rogsch, A. Schadschneider, and M. Schreckenberg (Springer, Heidelberg/Dordrecht/London/New York, 2010).

[19] T. Kretz, A. Grünebohm, M. Kaufman, F. Mazur, and M. Schreckenberg, J. Stat. Mech. (2006) P10001.
[20] S. K. Baek, P. Minnhagen, S. Bernhardsson, K. Choi, and B. J. Kim, Phys. Rev. E **80**, 016111 (2009).
[21] K. Sridhar and K. Bicha, Int. J. Sci. Eng. Tech. Res. **06**, 0638 (2017).
[22] K. Schmidt-Nielsen, Sci. Am. **200**, 109 (1959).
[23] N. S. Proctor and P. J. Lynch, *Manual of Ornithology* (Yale University Press, New Have, CT, 1993).
[24] C. W. Gottschalk and M. Mylle, Science **128**, 594 (1958).
[25] H.-W. Lee, V. Popkov, and D. Kim, J. Phys. A: Math. Gen. **30**, 99 (1997).
[26] P. F. Arndt, T. Heinzel, and V. Rittenberg, J. Phys. A: Math. Gen. **31**, L45 (1998).
[27] M. R. Evans, D. P. Foster, C. Godreche, and D. Mukamel, Phys. Rev. Lett. **74**, 208 (1995).
[28] N. Rajewsky, T. Sasamoto, and E. R. Speer, Physica A **279**, 123 (2000).
[29] T. Sasamoto and D. Zagier, J. Phys. A: Math. Gen. **34**, 5033 (2001).
[30] B. Schmittmann and R. K. P. Zia, in *Phase Transitions and Critical Phenomena*, edited by C. Domb and J. Lebowitz (Academic Press, London, 1994), Vol. 17.
[31] V. Privman, *Nonequilibrium Statistical Mechanics in One Dimension* (Cambridge University Press, Cambridge, UK, 1997).
[32] J. Marro and R. Dickman, *Nonequilibrium Phase Transition in Lattice Models* (Cambridge University Press, Cambridge, UK, 1999).
[33] G. M. Schütz, in *Phase Transitions and Critical Phenomena*, edited by C. Domb and J. Lebowitz, Vol. 19 (Academic Press, London, 2001), pp. 1–251.
[34] M. Henkel, H. Hinrichsen, and S. Lübeck, *Non-Equilibrium Phase Transitions: Volume 1: Absorbing Phase Transitions* (Springer, Netherlands, 2008).
[35] M. Henkel and M. Pleimling, *Non-Equilibrium Phase Transitions: Volume 2: Ageing and Dynamical Scaling Far from Equilibrium* (Springer, Netherlands, 2010).
[36] B. Derrida, S. A. Janowsky, J. L. Lebowitz, and E. R. Speer, J. Stat. Phys. **73**, 813 (1993).
[37] M. R. Evans, Y. Kafri, H. M. Koduvely, and D. Mukamel, Phys. Rev. Lett. **80**, 425 (1998).
[38] R. Lahiri and S. Ramaswamy, Phys. Rev. Lett. **79**, 1150 (1997).
[39] M. R. Evans, Y. Kafri, E. Levine, and D. Mukamel, J. Phys. A: Math. Gen. **35**, L433 (2002).
[40] K. Mallick, J. Phys. A: Math. Gen. **29**, 5375 (1996).
[41] B. Derrida and M. R. Evans, J. Phys. A: Math. Gen. **32**, 4833 (1999).
[42] M. R. Evans, Braz. J. Phys. **30**, 42 (2000).
[43] D. Mukamel, in *Soft and Fragile Matter: Nonequilibrium Dynamics, Metastability and Flow*, edited by M. E. Cates and M. R. Evans (IOP Publishing, Bristol, UK, 2000).
[44] M. R. Evans, Europhys. Lett. **36**, 13 (1996).
[45] J. Krug and P. A. Ferrari, J. Phys. A: Math. Gen. **29**, L465 (1996).
[46] R. A. Blythe and M. R. Evans, J. Phys. A: Math. Theor. **40**, R333 (2007).
[47] F. Spitzer, Adv. Math. **5**, 246 (1970).
[48] M. R. Evans and T. Hanney, J. Phys. A: Math. Gen. **38**, R195 (2005).
[49] O. J. O'Loan, M. R. Evans, and M. E. Cates, Europhys. Lett. **42**, 137 (1998).
[50] O. J. O'Loan, M. R. Evans, and M. E. Cates, Phys. Rev. E **58**, 1404 (1998).
[51] D. Chowdhury and R. C. Desai, Eur. Phys. J. B **15**, 375 (2000).
[52] M. Bando, K. Hasebe, A. Nakayama, A. Shibata, and Y. Sugiyama, Phys. Rev. E **51**, 1035 (1995).
[53] T. S. Komatsu and S.-i. Sasa, Phys. Rev. E **52**, 5574 (1995).
[54] H. Hayakawa and K. Nakanishi, Phys. Rev. E **57**, 3839 (1998).
[55] Y. Igarashi, K. Itoh, K. Nakanishi, K. Ogura, and K. Yokokawa, Phys. Rev. Lett. **83**, 718 (1999).
[56] F. Wilczek, Phys. Rev. Lett. **109**, 160401 (2012).
[57] A. Shapere and F. Wilczek, Phys. Rev. Lett. **109**, 160402 (2012).
[58] H. Watanabe and M. Oshikawa, Phys. Rev. Lett. **114**, 251603 (2015).
[59] N. Y. Yao, A. C. Potter, I.-D. Potirniche, and A. Vishwanath, Phys. Rev. Lett. **118**, 030401 (2017).
[60] D. V. Else, C. Monroe, C. Nayak, and N. Y. Yao, Annu. Rev. Condens. Matter Phys. **11**, 467 (2020).
[61] J. Szavits-Nossan and K. Uzelac, J. Stat. Mech. (2011) P05030.
[62] H. C. Berg, *E. coli in Motion* (Springer-Verlag, LLC, New York, 2004).
[63] D. R. Brumley, F. Carrara, A. M. Hein, Y. Yawata, S. A. Levin, and R. Stocker, Proc. Natl. Acad. Sci. USA **116**, 10792 (2019).
[64] J. Tailleur and M. E. Cates, Phys. Rev. Lett. **100**, 218103 (2008).
[65] M. E. Cates and J. Tailleur, Annu. Rev. Condens. Matter Phys. **6**, 219 (2015).
[66] E. Fodor and M. C. Marchetti, Physica A **504**, 106 (2018).
[67] A. G. Thompson, J. Tailleur, M. E. Cates, and R. A. Blythe, J. Stat. Mech. (2011) P02029.
[68] R. Soto and R. Golestanian, Phys. Rev. E **89**, 012706 (2014).
[69] A. B. Slowman, M. R. Evans, and R. A. Blythe, Phys. Rev. Lett. **116**, 218101 (2016).
[70] K. Malakar, V. Jemseena, A. Kundu, K. Vijay Kumar, S. Sabhapandit, S. N. Majumdar, S. Redner, and A. Dhar, J. Stat. Mech. (2018) 043215.
[71] E. Mallmin, R. A. Blythe, and M. R. Evans, J. Stat. Mech. (2019) 013204.
[72] A. Das, A. Dhar, and A. Kundu, J. Phys. A: Math. Theor. **53**, 345003 (2020).
[73] I. Mukherjee, A. Raghu, and P. K. Mohanty, arXiv:2208.05937.
[74] S. Jose, D. Mandal, M. Barma, and K. Ramola, Phys. Rev. E **105**, 064103 (2022).
[75] R. Dandekar, S. Chakraborti, and R. Rajesh, Phys. Rev. E **102**, 062111 (2020).
[76] A. K. Chatterjee and H. Hayakawa, SciPost Phys. **14**, 016 (2023).
[77] L. Turner, W. S. Ryu, and H. C. Berg, J Bacteriol. **182**, 2793 (2000).
[78] M. Sidortsov, Y. Morgenstern, and A. Be'er, Phys. Rev. E **96**, 022407 (2017).
[79] A. Be'er and G. Ariel, Mov. Ecol. **7**, 9 (2019).
[80] P. F. Arndt, T. Heinzel, and V. Rittenberg, J. Phys. A: Math. Gen. **31**, 833 (1998).
[81] P. F. Arndt, T. Heinzel, and V. Rittenberg, J. Stat. Phys. **97**, 1 (1999).